

1 **Improved constraints on transit-time**  
2 **distributions from Argon 39:**  
3 **A maximum-entropy approach**

*Submitted to JGR–Oceans*

Mark Holzer<sup>1</sup>

4 Department of Applied Mathematics, School of Mathematics and Statistics,  
5 University of New South Wales, NSW 2052, Australia.

François W. Primeau

6 Department of Earth System Science, University of California, Irvine, CA.

---

Mark Holzer, Department of Applied Mathematics, School of Mathematics and Statistics,  
University of New South Wales, Sydney, NSW 2052, Australia (mholzer@unsw.edu.au)

François W. Primeau, Department of Earth System Science, 3216 Croul Hall, University of  
California, Irvine, CA 92697-3100 (fprimeau@uci.edu)

<sup>1</sup>Also at Department of Applied Physics and  
Applied Mathematics, Columbia University,  
New York, NY.

**Abstract.** We use  $^{39}\text{Ar}$  in conjunction with CFCs, natural radiocarbon, and the cyclostationary tracers  $\text{PO}_4^*$ , temperature, and salinity to estimate the ocean's transit-time distributions (TTDs). A maximum-entropy method is employed to deconvolve the tracer data for the TTDs. The constraint provided by the  $^{39}\text{Ar}$  data allows us to estimate TTDs even in the deep Pacific where CFCs have not yet penetrated. From the TTDs we calculate the ideal mean age,  $\Gamma$ , the TTD width,  $\Delta$ , and the mass fraction of water with transit times less than a century,  $f_1$ . We also quantify the entropic uncertainties due to the nonuniqueness of the deconvolutions. In the Atlantic the patterns of  $\Gamma$  and  $f_1$  reflect the distribution of the major water masses. At the deepest locations in the North Atlantic  $\Gamma \simeq 300^{+300}_{-100}$  a, while at the deepest locations in the South Atlantic  $\Gamma \simeq 500^{+200}_{-100}$  a. The Pacific is nearly homogeneous below 2000 m with  $\Gamma \simeq 1300^{+200}_{-50}$  a in the North Pacific and  $\Gamma \simeq 900^{+200}_{-100}$  a in the deep South Pacific. The Southern Ocean locations have little vertical structure, with  $\Gamma$  ranging from 300 to 450 a with an uncertainty of about  $^{+150}_{-40}$  a. The importance of diffusion compared to advection as quantified by  $\Delta/\Gamma$  has most probable values ranging from 0.2 to 3., but with large entropic uncertainty bounds ranging from 0.2 to 9. For the majority of locations analyzed, the effect of  $^{39}\text{Ar}$  is to reduce  $f_1$  and to correspondingly increase  $\Gamma$  by about a century. The additional constraint provided by  $^{39}\text{Ar}$  reduces the entropic uncertainties of  $f_1$  by roughly 50% on average.

## 1. Introduction

7 Transport from the mixed layer into the ocean interior is fundamentally quantified by  
8 the boundary-propagator Green function,  $\mathcal{G}$ , an integral representation of the ocean's  
9 transport operator for transport from the surface. (We emphasize that the real ocean has  
10 a transport operator, not just ocean models.) Because the tracer concentrations at an  
11 interior point are convolutions in time and space of the mixed-layer concentrations with the  
12 boundary propagator, tracer measurements in the ocean interior provide data constraints  
13 on  $\mathcal{G}$ , and hence on oceanic transport from the surface. Here we apply a maximum-  
14 entropy (ME) method to hydrographic bottle data to deconvolve for  $\mathcal{G}$ . Physically, every  
15 fluid element in the bottle carries the tracer concentration of the mixed layer from the time  
16 and place when the fluid element was last in contact with the surface. The concentration  
17 measured for the bottle represents an admixture of these fluid elements, each of which has  
18 taken a different advective-diffusive path, with a different transit time, from the surface  
19 to the bottle. When integrated globally or regionally over source locations, the boundary  
20 propagator reduces to the transit-time distribution (TTD), which is the distribution of  
21 the transit times from the surface represented by the collection of fluid elements in the  
22 bottle.

23 Deconvolution of tracer data for the boundary propagator at a given point in the ocean  
24 interior is highly under-determined: For a given interior bottle location  $\mathcal{G}$  must be deter-  
25 mined for each time and location of possible last surface contact using only a few tracers,  
26 typically sampled sparsely in time and space. In particular, only a few tracers constrain  
27 the transit-time dependence of  $\mathcal{G}$ . For global coverage the Chlorofluorocarbons (CFCs)  
28 and radiocarbon are the only readily available candidates, although the CFC's have not

penetrated into the deep ocean everywhere. The CFC's and radiocarbon encode timescales that are separated by two orders of magnitude, with CFC's only going back some 70 years with an effective half-life of approximately 30 years and radio carbon with a half-life of 5730 years. The cosmogenically produced radio isotope  $^{39}\text{Ar}$  with a half-life of 269 years, roughly placed near the geometric mean of the CFC and radiocarbon timescales, is therefore an attractive tracer to bridge the gap in CFC and radiocarbon timescales. Because of its low abundance, traditional methods of determining the  $^{39}\text{Ar}$  concentration require large water volumes, and available data are therefore sparse. Nevertheless, new analytic techniques [e.g., *Gaelens et al.*, 2005] may make  $^{39}\text{Ar}$  concentrations more widely available and it is worth quantifying how estimates of  $\mathcal{G}$  are improved when  $^{39}\text{Ar}$  is available. In this paper we ask the following key questions:

1. *What do the deconvolutions of oceanic tracers, including  $^{39}\text{Ar}$ , reveal about ocean transport in terms of basic diagnostics such as ideal mean age, and the mass fraction of water in certain transit-time classes?*
2. *How does the inclusion of  $^{39}\text{Ar}$  change the results of maximum-entropy deconvolutions of TTDs and what are the systematics of these changes?*
3. *To what degree does the additional information carried by  $^{39}\text{Ar}$  reduce the uncertainty associated with the underdetermined nature of the deconvolution problem?*

To this end we apply ME deconvolutions to the  $^{39}\text{Ar}$  data obtained by *Loosli* [1989] as tabulated in the thesis of *Rodriguez* [1993], in conjunction with CFCs and natural (“pre-bomb”) radiocarbon from the GLODAP data set [*Key et al.*, 2004; *Sabine et al.*, 2005], and potential temperature,  $\theta$ , salinity,  $S$ , and the quasi-conserved tracer  $\text{PO}_4^* \equiv \text{PO}_4 + \text{O}_2/175$

51 [Broecker *et al.*, 1998] as computed from the World Ocean Atlas 2005 [WOA05, Locarnini  
52 *et al.*, 2006; Antonov *et al.*, 2006; Garcia *et al.*, 2006a, b].

53 The value of  $^{39}\text{Ar}$  as a transport tracer has been recognized in previous studies. *Maier-*  
54 *Reimer* [1993] used a simple argument based on one-dimensional advection-diffusion to  
55 interpret the  $^{39}\text{Ar}$ - $^{14}\text{C}$  scatter diagram as carrying distinct signatures for advective and  
56 diffusive transport. *Broecker and Peng* [2000] contrast  $^{39}\text{Ar}$  and  $^{14}\text{C}$  ages in the deep  
57 ocean assuming two end members whose proportions were inferred from the distribution  
58 of  $\text{PO}_4^*$  and attribute the difference between these tracer ages to diffusive mixing. Our  
59 approach emphasizes the estimation of tracer-independent transport diagnostics intrinsic  
60 to the flow by deconvolving tracer concentrations for the ocean's boundary propagator.

## 2. Deconvolution method

61 The ME method as applied to deconvolving tracer data to determine the boundary  
62 propagator was described in detail in the work of *Holzer et al.* [2010], which we now  
63 summarize: The concentration  $C_j^I(\mathbf{r}, t)$  of passive tracer species  $j$  at  $(\mathbf{r}, t)$  is the admixture  
64 of surface concentrations from surface points  $\mathbf{r}_s$  at earlier times  $t'$  given by the convolution

$$65 \quad C_j^I(\mathbf{r}, t) = \int d^2r_s \int_{-\infty}^t dt' \mathcal{G}(\mathbf{r}, t | \mathbf{r}_s, t') C_j^S(\mathbf{r}_s, t') e^{-\gamma_j(t-t')} , \quad (1)$$

66 where the boundary-propagator Green function  $\mathcal{G}$  is an integral representation of the  
67 transport from the surface [e.g., *Holzer and Hall*, 2000], and  $\gamma_j$  is the decay constant  
68 for radioactive species ( $\gamma_j = 0$  for non-radioactive species). The superscripts  $I$  and  $S$   
69 emphasize interior and surface tracer concentrations, respectively. Assuming the ocean to  
70 be cyclostationary and discretizing time into 12 month per year, the discretized version

of  $\mathcal{G}d^2r_s dt'$  is the probability  $\mathcal{P}(s, n, m|\mathbf{r}, m_0)$ . In terms of  $\mathcal{P}$  the convolution (1) becomes

$$C_j^I(\mathbf{r}, t) = \sum_s \sum_{n=0}^{\infty} \sum_{m=1}^{M(n)} \mathcal{P}(s, m, n|\mathbf{r}, m_0) C_j^S(s, t - \tau_{n,m}) e^{-\gamma_j \tau_{n,m}}$$

$$\equiv \hat{C}_j^I[\mathcal{P}] , \quad (2)$$

where  $\tau_{n,m} = [n + (m_0 - m)/12]\tau_a$  with  $\tau_a = 1a$  and  $M(0) = m_0$  and  $M(n) = 12$  for  $n > 0$ . Equation (2) also defines the notation  $\hat{C}_j^I[\mathcal{P}]$  for the value of the interior tracer concentration obtained by propagating the boundary conditions  $C_j^S$  with a given  $\mathcal{P}$ . Physically,  $\mathcal{P}(s, n, m|\mathbf{r}, m_0)$  is the mass fraction of water at  $\mathbf{r}$  during month  $m_0$  that had last contact with the  $s^{\text{th}}$  surface patch  $n$  years previously during month  $m$ , and thus had a transit time  $\tau_{n,m}$  from the surface to the point of observation. Equivalently,  $\mathcal{P}(s, n, m|\mathbf{r}, m_0)$  is the probability that a fluid element at  $\mathbf{r}$  had a transit time  $\tau_{m,n}$  since last surface contact with patch  $s$ , conditional on the fluid element currently being at  $\mathbf{r}$  during month-of-year  $m_0$ . To account for all the water at  $(\mathbf{r}, m_0)$ ,  $\mathcal{P}$  has the normalization  $\sum_{s,n,m} \mathcal{P}(s, m, n|\mathbf{r}, m_0) = 1$ . For less cumbersome notation below, we will also use the abbreviated notation  $\mathcal{P}(s, \tau|\mathbf{r}) \equiv \mathcal{P}(s, n, m|\mathbf{r}, m_0)$ .

## 2.1. Information entropy, $\mathcal{S}$

Following [Jaynes, 1957], we now assert that the best choice for  $\mathcal{P}$  is that which is maximally noncommittal with regard to missing information by maximizing the information entropy  $\mathcal{S}$  [Shannon, 1951] subject to any data constraints. Enforcing the data constraints with Lagrange multipliers  $\lambda_j$ , the information entropy of  $\mathcal{P}$  takes the form

$$\mathcal{S} = - \sum_{s,n,m} \mathcal{P} \log \frac{\mathcal{P}}{\mu} + \sum_{j=1}^J \lambda_j (C_j^I - \hat{C}_j^I[\mathcal{P}]) . \quad (3)$$

In (3) the measure, or ‘‘prior’’,  $\mu$  provides a prior guess at  $\mathcal{P}$  in the sense that the maximum of  $\mathcal{S}$  in the absence of data constraints is  $\mathcal{P} = \mu$ . By setting the functional derivative of

92  $\mathcal{S}$  with respect to  $\mathcal{P}$  to zero it follows that  $\mathcal{S}$  is maximized by

$$93 \quad \mathcal{P} = \frac{\mu}{Z} \exp \left( - \sum_j \lambda_j C_j^S(s, t - \tau_{n,m}) e^{-\gamma_j \tau_{n,m}} \right) , \quad (4)$$

94 where  $Z$  normalizes  $\mathcal{P}$ . The  $J$  Lagrange multipliers are found by substituting (4) into the  
 95  $J$  constraints (2). This results in equations that are nonlinear in the  $\lambda_j$ , that are then  
 96 solved numerically. (Note that while the normalization of  $\mathcal{P}$  could formally be imposed  
 97 with an additional Lagrange multiplier, normalizing the ME solution subject to only the  
 98 data constraints is mathematically equivalent.)

99 As in the work of *Holzer et al.* [2010], we consider both a uniform prior and a prior  
 100 based on coarse-resolution solutions of a steady advection-diffusion equation. We refer to  
 101 the latter as the advective-diffusive (AD) prior. The uniform prior has the property that  
 102 in the absence of any information all surface locations and all times since last contact, up  
 103 to a maximum time  $\tau_{\max} = 20000\text{a}$ , are equally likely. The details of how the priors were  
 104 constructed can be found in *Holzer et al.* [2010]. Additional details on how transit-time  
 105 was discretized is provided in Appendix A.

## 2.2. Entropic Distribution

106 To quantify the uncertainty associated with the underdetermined nature of finding  
 107  $\mathcal{P}$ , one must be able to assign a probability to functions  $\mathcal{P}$  that do not maximize the  
 108 constrained entropy, but that still satisfy the data constraints. We assume here that the  
 109 uncertainty associated with the underdetermined nature of the inversion is the dominant  
 110 uncertainty and ignore instrumental error and uncertainty due to temporal variability in  
 111 the data. Support for this assumption has been provided by Monte-Carlo simulations of  
 112 ME inversions of WOCE line A20 data [*Holzer et al.*, 2010]. In the case of negligible data

113 uncertainty the probability distribution of  $\mathcal{P}$  can be argued [e.g., *Skilling and Gull*, 1991;  
114 *Press et al.*, 2007] to take the form

$$115 \quad p(\mathcal{P}) \propto \exp\left(-\frac{N \mathcal{S}[\mathcal{P}]}{2 \mathcal{S}_{\max}}\right), \quad (5)$$

116 where  $\mathcal{S}_{\max}$  is the maximum of the data-constrained entropy, and  $N$  is the number of effec-  
117 tive constraints on  $\mathcal{P}$  provided by the data. Equating  $N$  with the number of constraints  
118 [e.g., *Gull and Daniell*, 1978] is the choice of the so-called “classic” maximum-entropy  
119 method [e.g., *Skilling and Gull*, 1991]. Here we take  $N = J$ , the number of tracer con-  
120 straints used. Thus, when all the tracers considered ( $T$ ,  $S$ ,  $\text{PO}_4^*$ , CFC-11, CFC-12,  $^{14}\text{C}$ ,  
121 and  $^{39}\text{Ar}$ ) are available for a given location,  $N = 7$ .

122 Typically we wish to determine the probability density function (pdf) of a di-  
123 agnostic  $\hat{D}[\mathcal{P}]$  that can be obtained as a moment of  $\mathcal{P}$ , that is,  $\hat{D}[\mathcal{P}] =$   
124  $\sum_{s,n,m} \mathcal{P}(s, n, m | \mathbf{r}, m_0) F(s, n, m)$ , for a suitable function  $F(s, n, m)$ . An example is  
125  $\hat{D} = \Gamma$ , the ideal mean age for which  $F = \tau_{n,m}$ . The pdf of  $\hat{D}$  taking a particular  
126 value in the interval  $(D, D + dD)$  is given by Eq. (5), where the entropy  $\mathcal{S}[\mathcal{P}]$  is computed  
127 for a propagator  $\mathcal{P}$  that is forced to satisfy the additional constraint that  $D = \hat{D}[\mathcal{P}]$ ,  
128 which we add to the constraints of Eq. (3) with the additional Lagrange multiplier term  
129  $\lambda_D(D - \hat{D})$ . (The maximum data-constrained entropy,  $\mathcal{S}_{\max}$  corresponds to the value of  
130  $D$  for  $\lambda_D = 0$ .)

131 Finding  $p(D)$  requires solving  $J + 1$  nonlinear equations for the Lagrange multipliers  
132 for each value of  $D$ . To reduce the computational burden, we proceed as in [*Holzer et al.*,  
133 2010] and compute the entropy  $\mathcal{S}(D)$  only at two values of  $D$  on each side of the ME  
134 value of  $D^*$  and use these points to fit  $\mathcal{S}$  to a power law  $\mathcal{S} = b|D - D^*|^a$  separately  
135 on each side of the maximum. We summarize the width of  $p(D)$  in terms of half-width

136 and probability-based error bars. The half-width error bar stretches from the left to  
 137 the right half-peak value of  $p(D)$ . The probability-based error bar stretches from  $D_L$   
 138 to  $D_R$ , where  $\int_{-\infty}^{D_L} p(D)dD = 0.5 \int_{-\infty}^{D^*} p(D)dD$ , and  $\int_{D_R}^{\infty} p(D)dD = 0.5 \int_{D^*}^{\infty} p(D)dD$ . In  
 139 other words the probability error bars stretch from half the cumulative probability to the  
 140 left of the ME value  $D^*$  to half the cumulative probability to the right of  $D^*$ . For a  
 141 symmetric distribution  $D_L$  and  $D_R$  locate the left and right quartiles of the distribution.  
 142 In all cases, the probability of  $D$  lying in the range of the probability error bar is 0.5, that  
 143 is,  $\int_{D_L}^{D_R} p(D)dD = 0.5$ . For convenience, we refer to the probability-based error bars as  
 144 quartile error bars, even in the case of asymmetric distributions.

### 3. Data

145 The  $^{39}\text{Ar}$  data used in this study was taken from the doctoral thesis of *Rodriguez* [1993],  
 146 which tabulates 125  $^{39}\text{Ar}$  measurements taken by Hugo Loosli and collaborators during  
 147 the 1980's and early 1990's. The data is sparse because the low abundance of  $^{39}\text{Ar}$  required  
 148 thousand-liter samples for the counting of electrons produced by the radioactive decay at  
 149 a rate of only a few per hour for surface water samples. The analytical techniques are  
 150 discussed by *Loosli* [1983] and the data is discussed by *Schlitzer et al.* [1985] and *Rodriguez*  
 151 [1993]. The data are in the form of the ratio of  $^{39}\text{Ar}$  to total Ar in the water sample relative  
 152 to the  $^{39}\text{Ar}/\text{Ar}$  ratio in the atmosphere, that is,  $\chi_{\text{Ar}} \equiv (^{39}\text{Ar}/\text{Ar})_{\text{sample}} / (^{39}\text{Ar}/\text{Ar})_{\text{atmos.}}$ ,  
 153 and carries a typical uncertainty of about 5%. Because of the rapid air-sea exchange of  
 154 argon, solubility plays no role and the surface can be considered to be saturated [e.g.,  
 155 *Maier-Reimer*, 1993]. We therefore treat  $\chi_{\text{Ar}}$  as a passive tracer with a surface boundary  
 156 condition of  $\chi_{\text{Ar}} = 1$ , independent of surface location. Because the focus of this study is

157 on the constraints provided by  $^{39}\text{Ar}$ , we perform the ME inversions at the locations where  
158 the water samples analyzed for  $^{39}\text{Ar}$  data were obtained.

159 The other time-dependent tracers employed are CFC-11, CFC-12, and natural (“pre-  
160 bomb”)  $^{14}\text{C}$ , whose annual mean interior and surface concentrations are taken from the  
161 GLODAP data set [*Key et al.*, 2004; *Sabine et al.*, 2005]. For the surface boundary  
162 conditions, the smaller GLODAP domain was extended to that of the WOA05 domain,  
163 as described by *Holzer et al.* [2010]. Where gridded CFC concentrations fell below the  
164 detection limit, the CFC data was not used. The time-evolving CFC boundary conditions  
165 were constructed as in the study of *Holzer et al.* [2010] by scaling the nominal 1994  
166 GLODAP surface values to the other years using the time series of atmospheric CFC  
167 concentrations [*Walker et al.*, 2000]. Temperature, salinity, phosphate, and oxygen data  
168 were taken from the World Ocean Atlas 2005 [WOA05, *Locarnini et al.*, 2006; *Antonov*  
169 *et al.*, 2006; *Garcia et al.*, 2006a, b], with annual means for the interior concentrations,  
170 and monthly means for the surface boundary conditions.

171 Argon data whose location fell outside the GLODAP domain were not considered. We  
172 also did not consider data in the upper 250m of the ocean because our neglect of seasonal  
173 and interannual variability in the CFC and  $^{14}\text{C}$  boundary conditions is particularly trou-  
174 blesome in the upper ocean. This leaves 70  $^{39}\text{Ar}$  measurements for which the other tracers  
175 are also available. The geographical locations of the tracer data sets used in this study  
176 are plotted in Fig. 1. Of these we could not find a numerically exact maximum entropy  
177 inversion for 9 data points because of either data inconsistencies (no linear combination  
178 of the boundary values can result in the interior values) or numerical difficulties. We thus

179 present results for 61 sets of tracer data, comparable to the number of  $^{39}\text{Ar}$  data that  
 180 were analyzed by *Broecker and Peng* [2000].

#### 4. One-dimensional idealized model

181 Before analyzing the oceanographic data it is useful to consider a simple one-dimensional  
 182 (1d) model to illustrate the role of  $^{39}\text{Ar}$  in constraining TTDS and to provide a sense of  
 183 the nature of the solutions and the entropic uncertainty.

184 The boundary conditions at the sea-surface for the four time-dependent tracers CFC-  
 185 11, CFC-12,  $^{14}\text{C}$ , and  $^{39}\text{Ar}$  are specified as follows: For the CFCs we use the globally  
 186 averaged atmospheric concentrations taken from the work of *Walker et al.* [2000], scaled  
 187 to some suitable mixed-layer concentration, which is arbitrary here. For  $^{14}\text{C}$ , and  $^{39}\text{Ar}$   
 188 we have  $C_j^S(\tau) = \exp(-\gamma_j\tau)$ , where the decay rate constant  $\gamma_j = \ln(2)/t_j^*$ , with half lives  
 189  $t_{\text{Ar}}^* = 269\text{a}$  and  $t_{\text{C}}^* = 5730\text{a}$ . These idealized boundary conditions are shown in Figure 2.  
 190 Note that the surface concentration of the CFCs is identically zero for  $\tau > 70\text{a}$ , which has  
 191 consequences for the inversions as discussed below.

192 Synthetic interior tracer concentrations were generated by convolving these boundary  
 193 conditions with a model boundary propagator that is independent of surface location,  
 194 that is, with a model TTD. The natural choice is an inverse Gaussian (IG),  $\mathcal{G}_{\text{IG}}$ , which is  
 195 also a solution to the 1d advection diffusion equation [e.g., *Hall and Plumb*, 1994]. The  
 196 IG is a function of two parameters, its mean age  $\Gamma$  and its width  $\Delta$ . The mean age  
 197 parameter can be thought of as being proportional to depth,  $z$ : For constant-coefficient  
 198 advection-diffusion with advection speed  $v$  one has  $z = v\Gamma$ . The mode of  $\mathcal{G}_{\text{IG}}$ , that is,  
 199 the time  $\tau_m$  for which  $\mathcal{G}_{\text{IG}}$  is peaked is given by  $\tau_m = (\sqrt{1 + (3/\text{Pe}^2)^2} - 3/\text{Pe}^2)\Gamma$ , where  
 200  $\text{Pe} \equiv \Gamma/\Delta$  is the Péclet number of the 1d flow.

201 Given the boundary conditions and the synthetic data for a given  $\Gamma$  and  $Pe$ , we can  
 202 then imagine that the boundary propagator is unknown and use the ME-deconvolution  
 203 to provide an estimate for  $\mathcal{G}$ , which can then be compared against the true answer, our  
 204 assumed IG. The ME deconvolutions for this 1d model were performed using a uniform  
 205 prior out to  $\tau = 20000a$ .

206 Figure 3 shows the deconvolved TTDS with and without  $^{39}\text{Ar}$  compared to the true  
 207 model  $\mathcal{G}_{\text{IG}}$  for  $Pe = 1.5$  and  $Pe=10$ . A value of  $Pe=1.5$  is thought to be typical of the real  
 208 ocean [e.g., *Waugh et al.*, 2004, and see below], while  $Pe=10$  represents more advectively  
 209 dominated flow. The main message of the figure is that without  $^{39}\text{Ar}$ , the ME solution  
 210 for the TTD cannot form a mode beyond the CFC period of  $\sim 70a$ : Without  $^{39}\text{Ar}$  the tail  
 211 of the ME solution for  $\tau > 70a$  is determined only by  $^{14}\text{C}$ , and because the TTD must  
 212 approach zero for large  $\tau$  the Lagrange multiplier of  $^{14}\text{C}$  must be positive, which implies  
 213 that the TTD decreases monotonically for  $\tau > 70 a$ . On the other hand if both  $^{39}\text{Ar}$   
 214 and  $^{14}\text{C}$  are available, the Lagrange multipliers of the two tracers can be of opposite sign,  
 215 allowing the solution to have both growth and ultimate long- $\tau$  decay beyond the CFC  
 216 period so that a mode at long  $\tau$  is possible. This is particularly evident for  $Pe=10$ , but  
 217 also visible at large mean ages for  $Pe=1.5$ .

218 Figure 3 allows us to emphasize another important point: Even with error-free tracer  
 219 data, such as used in this example, one cannot expect the ME deconvolutions to recover  
 220 the true underlying TTD with only a handful of tracer constraints. The ME solution is  
 221 the exponentiated linear combination of the surface values of the few available tracers  
 222 as expressed by Eq. (4). While this solution guarantees to satisfy the available tracer  
 223 constraints (2), constraining the functional shape of the TTD amounts to constraining

224 the TTD for an infinite number of transit times. (Alternatively, constraining the detailed  
 225 functional form of the TTD is equivalent to constraining an infinite number of its mo-  
 226 ments.) Thus, the ME deconvolution can only recover the underlying TTD exactly for an  
 227 infinite number of (independent) tracer constraints. The fact that the ME deconvolution  
 228 is able to provide an estimate of the functional form of the TTD with only a few tracer  
 229 constraints is due to the smoothing property of the entropy functional [e.g. *Press et al.*,  
 230 2007], which spreads out the probabilities  $\mathcal{P}$  as much as possible relative to the prior  $\mu$ .  
 231 The functional form of the ME deconvolutions (4) is not constrained to be unimodal and  
 232 is therefore in principle able to capture multimodal TTDs arising from multiple advective-  
 233 diffusive pathways. However, it must be kept firmly in mind that the functional shape  
 234 constrained by only a few tracer observations has significant uncertainty and the detailed  
 235 structure of the deconvolved TTD should not be over-interpreted as underscored by the  
 236 spurious bimodality of the inversion for  $Pe = 1.5$  and  $\tau_m = 25$  a ( $\Gamma = 75$ a) in Figure 3.  
 237 A key strength of the ME method is that we can quantitatively assess the uncertainty  
 238 associated with the paucity of constraints.

239 To illustrate the nature of the entropic uncertainty due to the underdetermined nature of  
 240 the deconvolutions, we focus on the mass fractions of water in the three transit-time bands  
 241  $[t_{min}, t_{max}) = [0, 100), [100, 500),$  and  $[500, 20000]$ a, where the mass fraction is simply  
 242  $f = \int_{t_{min}}^{t_{max}} d\tau \mathcal{G}(\tau)$ . We denote the mass fractions in the three bands  $f_1, f_2,$  and  $f_3,$  with  $f_1$   
 243 containing the youngest water, and  $f_3,$  the oldest. Note that  $f_1 + f_2 + f_3 = 1$ . Figure 4  
 244 shows the probability distributions for these fractions for  $Pe=1.5,$  as obtained with and  
 245 without  $^{39}\text{Ar}$  for five different modal times  $\tau_m$  (and hence five different ideal mean ages) of  
 246 the underlying assumed IG TTD. The pdfs of the water-mass fractions are generally quite

247 broad, except where the ME values of  $f$  lie near the extremes of  $f = 0$  or 1 (none or all the  
 248 water in the band). This broadness reflects the fact that we are using only three or four  
 249 data constraints to estimate a TTD of arbitrary functional form (as opposed to fixing the  
 250 functional form from the outset and estimating only a few parameters). Including  $^{39}\text{Ar}$   
 251 narrows the pdfs reflecting the additional constraint and the reduced entropic uncertainties  
 252 in the maximum-entropy values. Including  $^{39}\text{Ar}$  generally also changes the maximum-  
 253 entropy value, but these changes are small compared to the width of the pdfs.

254 To quantify the changes  $\delta f$  in the inferred water-mass fractions in each transit-time  
 255 band due to the inclusion of  $^{39}\text{Ar}$ , Fig. 5 shows these changes as a function of the true  
 256 ideal mean age,  $\Gamma$ , that is, the mean age of the assumed  $\mathcal{G}$ . Note that conservation of mass  
 257 demands  $\delta f_1 + \delta f_2 + \delta f_3 = 0$ . For waters with  $\Gamma \lesssim 750\text{a}$ , inclusion of  $^{39}\text{Ar}$  gives estimates  
 258 with less water in the mid- $\tau$  band, and correspondingly more water in the short- $\tau$  and  
 259 long- $\tau$  bands. For older ideal mean ages, inclusion of  $^{39}\text{Ar}$  increases the long- $\tau$  content of  
 260 the water at the expense of the mass fraction in the short- $\tau$  and mid- $\tau$  bands.

261 The ideal mean age of the deconvolved TTD is surprisingly close to the true mean age  
 262 of the assumed model transport. The discrepancy between inferred and true mean age  
 263 for  $\text{Pe} = 1.5$  is only about 2% when  $^{39}\text{Ar}$  is not used, and less than 1% when  $^{39}\text{Ar}$  is used.  
 264 Though less relevant for the real ocean, at  $\text{Pe} = 10$  the discrepancy without  $^{39}\text{Ar}$  can be  
 265 several percent for waters with young ideal mean ages, but with  $^{39}\text{Ar}$  becomes negligible  
 266 for  $\Gamma \gtrsim 150\text{a}$ .

## 5. Deconvolutions of hydrographic data

267 Because our focus here is on the utility of  $^{39}\text{Ar}$  for which the surface boundary conditions  
 268 were approximated as perfectly uniform, we consider here only the temporal structure of

269 the boundary propagator. In particular, we focus on the mass-fraction  $f_1$  of water younger  
270 than  $\tau_1 \sim 105$ a and on the mean and centered second moment of the distribution of transit  
271 times since last contact anywhere on the surface (TTD). (Note that the mass fraction older  
272 than  $\tau_1$  is simply  $1 - f_1$ .) We first present these diagnostics as computed using the AD prior  
273 and all available tracer constraints, including  $^{39}\text{Ar}$ , that is, we first analyze our results  
274 obtained using the maximum available information. We then systematically investigate  
275 the effect of  $^{39}\text{Ar}$  by comparing the diagnostics and their uncertainties computed with and  
276 without  $^{39}\text{Ar}$  and with each prior.

### 5.1. Oceanographic significance of the results with $^{39}\text{Ar}$

277 Figure 6 shows the inversion results for the mass fraction,  $f_1$ , of water with  $\tau \in [0, 105]$ a  
278 for all the bottles below 250m separately for the North Atlantic, South plus Equatorial  
279 Atlantic, Pacific and Southern-Ocean basins. To a first approximation, we can consider  
280 the plots to represent vertical profiles for each basin, but we note that for each basin data  
281 from all latitudes and longitudes has been collapsed onto a single plot. (Only for the  
282 Pacific does the data actually consist of three vertical profiles at the locations shown in  
283 Figure 1.)

284 The  $f_1$  profiles reveal important differences in the water-mass structure and ventila-  
285 tion pathways of the different basins. In the North Atlantic the vertical structure of  
286  $f_1$  as revealed by our inversions is consistent with what one expects given the known  
287 distribution of the ocean's major water masses. Relatively large values of  $f_1$  are found  
288 between  $\sim 2000$  and  $\sim 4000$ m depth, where North Atlantic Deep water (NADW) separates  
289 Antarctic Intermediate water (AAIW) above from Antarctic Bottom water (AABW) be-  
290 low. [These water-mass identifications were checked to be consistent with density (not

shown).] The longer transit time from the surface of the Southern Ocean to the North Atlantic for AAIW and AABW is reflected in the relatively smaller  $f_1$  values for the deepest bottles (AABW) and for the two bottles at 850m depth (AAIW). The data point with  $f_1 \sim 0.9$  at 680m depth comes from the center of the Labrador Sea, a well-known deep-water formation site where we expect to find recently ventilated water with  $f_1$  near unity. Consistent with the longer time needed for NADW to be transported into the South Atlantic, the values of  $f_1$  for the South and Equatorial Atlantic in the depth range where one would expect to find NADW has generally decreased from the corresponding North-Atlantic values. In contrast,  $f_1$  values at  $\sim 900$ m depth have increased, consistent with AAIW being closer to its source in the South and Equatorial Atlantic than in the North Atlantic. The Pacific profiles are consistent with the notion that the thermocline waters of the North Pacific are ventilated by subduction, downward Ekman pumping, and relatively shallow convection, whereas the deep Pacific waters are ventilated from remote deep-water formation sites in the Southern Ocean and North Atlantic. The Pacific  $f_1$  values are seen to decrease with depth down to about  $\sim 1000$ m below which  $f_1$  is near zero. For the profile near Baja California at ( $28.5^\circ\text{N}$ ,  $122.2^\circ\text{W}$ , grey squares), the values of  $f_1$  in the thermocline are significantly smaller than for the other two Pacific locations. The thermocline at the Baja location is thus relatively poorly ventilated, consistent with its proximity to the North-Pacific shadow zone [Luyten *et al.*, 1983; Gehrie *et al.*, 2006]. In the Southern Ocean, apart from a suggestion that  $f_1$  increases slightly with depth, the vertical structure is much more uniform than elsewhere. This is consistent with the fact that in the Southern Ocean we have both formation of deep waters and re-exposure of older waters to the atmosphere. The somewhat larger mass fraction in the youngest

314 transit-time band found for the deepest Southern-Ocean bottles, if taken at face value, is  
315 consistent with the ventilation of the bottom waters by shelf-slope convection along the  
316 Antarctic coast and subsequent upward mixing with older overlaying waters [e.g., *Foster*  
317 *and Carmack*, 1976; *Orsi et al.*, 1999].

318 Figure 7 shows our ME estimates for the ideal mean age,  $\Gamma$ , as a function of depth,  
319 again plotted separately for four ocean basins as in Figure 6. Both the results with and  
320 without  $^{39}\text{Ar}$  are shown so that the uncertainty reduction due to  $^{39}\text{Ar}$  can be seen. The  
321 smaller error bars obtained when  $^{39}\text{Ar}$  is included are particularly apparent in the Pacific  
322 and Southern Ocean. We note that while including ever more tracer constraints would  
323 ultimately lead to zero uncertainty, the approach to this limit with a nonuniform prior is  
324 not guaranteed to be monotonic and a few of the error bars actually increase when  $^{39}\text{Ar}$  is  
325 included. We now focus on the depth dependence of ideal mean age itself and then return  
326 in detail to the effect of  $^{39}\text{Ar}$  as an extra constraint in the next section.

327 The vertical structure of  $\Gamma$  seen in Figure 7 is broadly consistent with the structure that  
328 we saw for  $f_1$  in Figure 6. In the North Atlantic the youngest mean ages are found in  
329 the core of NADW between 2000 and 3000m. Water above and below this depth tends  
330 to have older mean ages consistent with AAIW and AABW, which must travel farther  
331 to reach the North Atlantic. In the South and Equatorial Atlantic, the youngest mean  
332 ages (where we have  $^{39}\text{Ar}$  data) are found above 1000m where one would expect to find  
333 AAIW (see also *Holzer et al.* [2010]). Mean ages in the South and Equatorial Atlantic  
334 tend to increase gradually with depth except perhaps below 4000m, where there is a  
335 sharp increase, but the large uncertainties preclude any firm conclusions. It is interesting  
336 to note that the deepest water masses tend to be older in the South Atlantic than in

337 the North Atlantic suggesting that there is a gradual entrainment of NADW as AABW  
 338 flows northward into the North Atlantic. In the Pacific we find mean ages that tend to  
 339 increase from a minimum at the surface to a maximum at a depth of  $\sim 2000\text{m}$ , below which  
 340 mean age remains fairly constant throughout the homogeneous deep Pacific water mass.  
 341 Consistent with the idea that the deep Pacific is ventilated from the south, the mean ages  
 342 tend to be younger in the South Pacific (blue squares) than in the North Pacific (black  
 343 and gray squares). Interestingly, the age profiles of the two North Pacific locations are  
 344 very similar in spite of their different  $f_1$  profiles. This is consistent with the fact that  
 345 the TTDs at  $(31.1^\circ\text{N}, 150^\circ\text{W})$  are significantly broader in the thermocline than those  
 346 near Baja California (see Fig. 8 discussed below). In contrast to the other basins, ideal  
 347 mean ages in the Southern Ocean are more uniform with depth again suggesting that the  
 348 Southern Ocean is an important location for the blending of different water masses, and  
 349 where deep waters are not only newly formed but where old waters are also re-exposed to  
 350 the surface.

351 Figure 8 shows the width,  $\Delta$ , of the TTD defined by  $2\Delta^2 = \int_0^\infty (\tau - \Gamma)^2 \mathcal{G}(\tau) d\tau$ . The  
 352 uncertainties of  $\Delta$  were estimated from the entropic uncertainties of  $m_2 \equiv \int_0^\infty \tau^2 \mathcal{G}(\tau) d\tau$   
 353 as described in Appendix B. Larger widths imply a greater multiplicity of transit times  
 354 from the sea surface. This can be achieved by having a larger multiplicity of paths and  
 355 transport timescales from a single water-mass formation region or by mixing water from  
 356 multiple source regions. As a general rule, one expects higher-order moments to be less  
 357 well constrained than lower-order moments ( $\Gamma$  being the first-order moment, or mean,  
 358 and  $2\Delta^2$  being the second-order moment). Consistent with this expectation,  $\Delta$  is seen  
 359 to have much greater uncertainty than  $\Gamma$ . Despite the large uncertainties, our inversions

360 suggest that the widths tend to increase with depth except perhaps for the Southern  
361 Ocean where  $\Delta$  is nearly uniform with depth. As a general rule of thumb, one expects a  
362 large correlation between  $\Gamma$  and  $\Delta$  because older water masses with large  $\Gamma$  have had more  
363 time to mix and thus to produce broader TTDS with larger values of  $\Delta$ . This correlation  
364 is seen most places, with the old deep waters of the Pacific and Atlantic having large  
365 values of  $\Delta$ , although the uncertainties for the Atlantic bottom waters are so large that  
366 their true width could be considerably smaller. An interesting exception to the rule is the  
367 thermocline waters of the North Pacific, where the values of  $\Delta$  are roughly the same as  
368 those at depth even though thermocline waters have much smaller mean age than deep  
369 waters. There is even a suggestion that the largest North-Pacific values of  $\Delta$  occur in  
370 the upper-most bottles analyzed, but the large uncertainties for these two bottles prevent  
371 definite conclusions. The weak dependence of  $\Delta$  on depth in the North Pacific in spite  
372 of the strong vertical gradients of  $\Gamma$  above 2000m suggests a subtle, complex structure of  
373 the TTDS in the North Pacific thermocline (see also Figure 10 below), perhaps resulting  
374 from upward diffusing older waters mixing with more recently ventilated water.

375 The ratio of  $\Delta/\Gamma$  is useful for characterizing the relative importance of diffusive and  
376 advective transport. If  $\Delta/\Gamma \ll 1$ , advection dominates over diffusion, while the converse  
377 is true if  $\Delta/\Gamma \gg 1$ . There have been few estimates of  $\Delta/\Gamma$  from transient tracer data  
378 in the ocean. The only studies we are aware of are those of *Waugh et al.* [2003] and  
379 *Hall et al.* [2004], where measurements of CFC-11 and CFC-12 were used in conjunction  
380 to constrain both  $\Gamma$  and  $\Delta$ . Because CFCs have relatively fast timescales, those studies  
381 could only estimate  $\Delta$  and  $\Gamma$  for the relatively young water masses of the upper ocean  
382 where measurable CFC concentrations are present. Because we are using  $^{39}\text{Ar}$  and  $^{14}\text{C}$

383 tracer data in addition to the CFC data, we are able to constrain  $\Gamma$  and  $\Delta$  for deep  
384 waters as well. Furthermore, the previously estimated values of  $\Delta/\Gamma$  were based on a  
385 parametric inversion approach in which the functional form of the TTD is assumed to  
386 be a two-parameter IG distribution that is completely specified given  $\Gamma$  and  $\Delta$ . The IG  
387 approach turns an under-determined problem into one that is exactly determined even  
388 with only two tracers whose timescales are similar. As such, the IG approach is poorly  
389 suited for quantifying what we call the entropic uncertainty, that is, the uncertainty in  
390  $\Delta/\Gamma$  associated with the fact that the functional form of the TTD is not known.

391 In Figure 9 we plot estimates of  $\Gamma/\Delta$  obtained from our ME inversions. (For convenience  
392 we plot  $\Gamma/\Delta$  and its error bars rather than  $\Delta/\Gamma$  so that a single scale suffices to show  
393 the error estimates in all basins.) While the corresponding ME estimates for  $\Delta/\Gamma$  are  
394 generally greater than 0.2, the uncertainty is large and we cannot rule out a value of  
395  $\Delta/\Gamma$  as low as 0.1 in some locations. Nevertheless, it is generally true that eddy-diffusive  
396 transport is significant everywhere and cannot be neglected. The so-called TTD method  
397 for estimating anthropogenic  $\text{CO}_2$  in the ocean [e.g., *Waugh et al.*, 2006] generally assumes  
398 a value of  $\Delta/\Gamma$  close to unity. Within the framework of this TTD method, *Waugh et al.*  
399 [2006] report that anthropogenic  $\text{CO}_2$  estimates are most sensitive to the assumed value  
400 of  $\Delta/\Gamma$  when  $\Delta/\Gamma$  is in the range between 0.2 and 0.8. For the upper ocean *Waugh et al.*  
401 [2006] show that the CFC data is sufficient to exclude this range, but for deeper water  
402 our results suggest that values of  $\Delta/\Gamma$  in the range between 0.2 and 0.8 cannot be ruled  
403 out.

404 In Figure 10 we plot the ME TTDs (black curves) for the North Pacific station at  
405 (28.5°N, 122.2°W, upper plot) and for the stations in the Southern Ocean (lower plot).

406 Superposed on each ME TTD is an IG distribution (red curves) with the same  $\Gamma$  and  
 407  $\Delta$  as the ME TTD. Only for the North Pacific profile below the thermocline is there  
 408 relatively good agreement between the IG distribution and the ME TTD. In the North  
 409 Pacific thermocline above 600m and for all depths in the Southern Ocean, the ME TTDs  
 410 have an additional mode for  $\tau \lesssim 50\text{a}$ , which is absent in the less flexible IG distribution.  
 411 It is difficult to know for certain if these short- $\tau$  modes are real or artifacts of the under-  
 412 determined nature of the inversion. However, their existence does not contradict what  
 413 is known about the ventilation of the ocean: In the North Pacific subduction of newly  
 414 ventilated water masses could easily explain the short- $\tau$  mode and in the Southern Ocean  
 415 one expects to find recently ventilated water masses close to the deep water formation  
 416 sites. It may be worth remarking that for most locations the TTDs of the corresponding  
 417 AD prior (not shown) bear little resemblance to the ME TTDs. Details on the character  
 418 of the AD prior TTDs may be found in the paper by *Holzer et al.* [2010].

## 5.2. The effect of $^{39}\text{Ar}$ as an extra constraint

419 We now turn our attention to comparing ME inversions with and without  $^{39}\text{Ar}$  to  
 420 quantify the effect of including  $^{39}\text{Ar}$  as an additional constraint. To this end, we focus on  
 421 four key quantities: The mass fraction of water in each of the three transit time bands  
 422 0–105, 105–550, 550–20000a (band 1, 2, and 3), and the ideal mean age  $\Gamma$ . We refer to  
 423 the three transit-time bands as the short- $\tau$ , mid- $\tau$ , and long- $\tau$  bands.

424 Figure 11 shows the effect of  $^{39}\text{Ar}$  on the inversions for the mass fraction in each transit-  
 425 time band as a function of the ideal mean age of the bottle (determined with  $^{39}\text{Ar}$ ).  
 426 Of particular interest is the Pacific, where inferred mean age increases approximately  
 427 monotonically with depth (Figure 7), mimicking 1d advection-diffusion. Comparison of

428 the Pacific panel of Figure 11 for the uniform prior with Figure 5 shows that the Pacific  
429 profiles and the idealized 1d model have broadly similar behavior in how the changes in  
430 water-mass fractions depend on ideal mean age. For the case of the uniform prior, this  
431 behavior may again be attributed to the fact that  $^{39}\text{Ar}$  gives the ME functional form of  
432 the TTD freedom to build a mode away from the CFC limit at  $\sim 70\text{a}$ . With the AD prior a  
433 clear pattern for the Pacific is not apparent, except that the largest changes occur for the  
434 bottles with the oldest ideal mean age, which contain generally more water in the long- $\tau$   
435 band with  $^{39}\text{Ar}$  than without. The Atlantic bottles are generally younger and hence there  
436 is little change in the long- $\tau$  band, which contains little water. When  $^{39}\text{Ar}$  is included, the  
437 dominant effect on the Atlantic bottles is an increase in the mass fraction in the mid- $\tau$   
438 band at the expense of the mass in the short- $\tau$  band, with less systematic behavior for  
439 the AD prior than for the uniform prior.

440 Figure 12 quantifies the reduction in the entropic uncertainty of the mass fractions  
441 in each of the three transit-time bands due to including  $^{39}\text{Ar}$  as an extra constraint.  
442 The uncertainty reduction is simply defined as the ratio,  $R$ , of the quartile error bar  
443 without  $^{39}\text{Ar}$  to the error bar with  $^{39}\text{Ar}$ . For the uniform prior, including  $^{39}\text{Ar}$  reduces the  
444 uncertainty ( $R > 1$ ) for essentially all bottles. The small amount of scatter below  $R = 1$   
445 is likely an artifact of approximating the entropic pdf of  $f_1$  by fitting it to two points on  
446 either side of the ME value (a five-point fit). For the AD prior it is very interesting to  
447 note that while the uncertainty is reduced ( $R > 1$ ) for most bottles, for some 18 bottles  
448 inclusion of  $^{39}\text{Ar}$  turns out to increase the uncertainty ( $R < 1$ ). We have closely examined  
449 our estimates of the entropic pdfs of  $f_1$  to ensure that the effect is not merely an artifact  
450 of our five-point fit, although the approximation likely accounts for some of the points

451 with  $R$  below unity by only a small amount ( $\sim 0.05$ ). We find that significant increases  
452 in uncertainty ( $R < 1$ ) can occur with the AD prior when the inversion without  $^{39}\text{Ar}$   
453 gives a ME value of  $f_1$  close to either extreme of  $f_1 = 0$  or  $f_1 = 1$ , which is then shifted  
454 significantly away from its extreme when  $^{39}\text{Ar}$  is included. We have yet to uncover the  
455 detailed mechanism by which a nonuniform prior can lead to uncertainty increases when  
456 an extra constraint is included, but we are able to reproduce the effect with the idealized  
457 1d model of section 4 when the prior consists of an IG distribution with a prior mean age  
458 that is significantly larger (by a factor of  $\sim 1.5$ ) than that of the true underlying boundary  
459 propagator.

460 The reductions in the uncertainty of the water-mass fractions averaged over the bottles  
461 for which  $R \geq 1$  are similar for the uniform and AD prior cases: approximately 50% for  
462 the short- $\tau$ , 20% for the mid- $\tau$ , and 30% for the long- $\tau$  band, with  $R$  exceeding a factor  
463 of two for about a dozen bottles. Including  $^{39}\text{Ar}$  thus provides the greatest constraint on  
464 the short and long-transit-time water-mass fractions. The dependence of the uncertainty  
465 reduction on ideal mean age,  $\Gamma$ , shows a great deal of scatter, but generally most bottles  
466 with  $\Gamma \gtrsim 700\text{a}$  show a significant reduction in uncertainty, while most bottles younger than  
467 that (largely from the Atlantic) have smaller uncertainty reductions.

468 The uncertainty reduction for ideal mean age,  $\Gamma$ , that results from including  $^{39}\text{Ar}$  as an  
469 extra constraint is evident in Figure 7, particularly for the Pacific and Southern Ocean  
470 locations. Detailed examination of the uncertainty reduction ratio showed that in the case  
471 of the AD prior about a dozen bottles, most in the Atlantic thermocline and abyss and  
472 four in the Pacific thermocline, again experience an increase in uncertainty when  $^{39}\text{Ar}$  is  
473 included. Some of the effect may be due to our 5-point approximation when the entropic

pdfs of  $\Gamma$  are highly skewed, but for most of these bottles the effect is likely similar to what was seen for the water-mass fractions. Importantly, however, for most locations  $^{39}\text{Ar}$  reduces the uncertainty in  $\Gamma$  with average reduction ratios of 1.3 in the Atlantic, 1.3 in the Pacific, and 2.0 in the Southern Ocean.

Figure 13 examines the changes in the mass fraction in the short- $\tau$  band,  $f_1$ , when  $^{39}\text{Ar}$  is included as an additional transient tracer. For nearly all bottles, and for both the uniform and AD priors, the short- $\tau$  fraction is substantially reduced except for the deep Pacific bottles that tend to be too old to contain much short- $\tau$  water. For the case of the uniform prior, the reduction in  $f_1$  is consistent with the additional degree of freedom afforded by  $^{39}\text{Ar}$ , which allows the TTD to have a mode beyond 70a, and hence less water with transit times within the CFC period. For the case of the AD prior with its non-trivial structure, there is no obvious mechanism that should lead to reduced  $f_1$  values. The outlier point for the AD-prior case that shows a large increase from  $f_1 = 0.15$  to  $f_1 = 0.92$  lies at  $37.3^\circ\text{N}$ ,  $45.4^\circ\text{W}$ , and 3970m depth in the North Atlantic. This point has similar behavior in the uniform-prior case with an increase from  $f_1 = 0.47$  to  $f_1 = 0.80$ , which does not show as prominently on the plot. An increase of  $f_1$  as the result of  $^{39}\text{Ar}$  as an extra constraint simply means that the observed  $^{39}\text{Ar}$  concentration is larger than expected on the basis of the other tracer constraints.

It is very interesting to note that the mass fractions obtained with  $^{39}\text{Ar}$  are roughly the same regardless of whether we use the uniform or AD prior. This is emphasized in the bottom panel of Figure 13 by plotting the inversions for  $f_1$  with the AD prior versus those using the uniform prior, both with  $^{39}\text{Ar}$ . The scatter around the diagonal is much smaller than the changes in  $f_1$  resulting from the inclusion of  $^{39}\text{Ar}$ . While we expect

497 that the choice of prior becomes secondary once enough data is used in the inversion, it  
498 is remarkable that just four transient tracers (CFC-11, CFC-12,  $^{14}\text{C}$ , and  $^{39}\text{Ar}$ ) already  
499 places the still highly under-determined inversions in a regime of insensitivity to the choice  
500 of prior.

501 The changes in the estimates of ideal mean age,  $\Gamma$ , that result from including  $^{39}\text{Ar}$  in  
502 the ME inversions are quantified in Figure 14 for the uniform and AD prior cases. (Only  
503 bottles with  $\Gamma \leq 500\text{a}$  are shown to make the changes more visible. For the older Pacific  
504 bottles, in the case of the AD prior, the changes in  $\Gamma$  are much smaller.) As expected  
505 from the reductions in the water-mass fractions with  $\tau < 105\text{a}$ , for most bottles the ideal  
506 mean age is estimated to be older when  $^{39}\text{Ar}$  is included. Note that this is not a statement  
507 about either the AD or uniform priors having a young bias. (In fact, the uniform prior has  
508 an old bias with a mean age of 10000a.) Instead, the inclusion of  $^{39}\text{Ar}$  corrects a young  
509 bias in the ME TTDs as constrained by all the other tracers. The bottom panel of Figure  
510 14 shows that for most locations the choice of prior is secondary for determining the ME  
511 value of  $\Gamma$  when  $^{39}\text{Ar}$  is included. This insensitivity to the choice of prior is similar to  
512 that seen for  $f_1$  in Figure 13 and is particularly striking in light of the fact that the ideal  
513 mean age of the uniform prior is 10000 a for all locations, while the AD prior has a more  
514 realistic distribution of ideal mean age [*Holzer et al.*, 2010].

## 6. Discussion

515 In this paper we quantified the extent to which  $^{39}\text{Ar}$  helps constrain specific diagnostic  
516 properties of the ocean's TTDs, namely ideal mean age, TTD width, and the water-  
517 mass fraction in specified transit-time bands. It is important to appreciate, however,  
518 that the value of any tracer constraint depends on the particular diagnostic property one

519 is interested in. For example, we found that  $^{39}\text{Ar}$  helped reduce the uncertainty in the  
520 water-mass fractions with short and long transit times, but had much less effect on the  
521 uncertainties in the 105–550a transit-time band even though this band brackets the  $^{39}\text{Ar}$   
522 decay timescale. The utility of a given transient tracer not only depends on its time  
523 dependence, but also critically on the spatial pattern of its surface boundary condition.  
524 Thus,  $^{39}\text{Ar}$  with its nearly uniform boundary condition is expected to be of little use  
525 in constraining where water was last ventilated. Conversely, the spatial structure of a  
526 tracer’s boundary condition has implications for estimating timescales. For example,  $^{14}\text{C}$   
527 with its very long decay timescale has a favorable temporal structure to constrain the  
528 ideal mean age, but its spatially inhomogeneous surface boundary condition is not well  
529 matched to the uniform boundary condition of the ideal mean age [*Holzer et al.*, 2010;  
530 *DeVries and Primeau*, 2010]. In contrast,  $^{39}\text{Ar}$  has a uniform boundary condition, but  
531 its faster decay projects less well onto the linear dependence desired to constrain mean  
532 age. The utility of  $^{39}\text{Ar}$  as a constraint will also depend on what other tracer constraints  
533 are available. In general, the incremental reduction in uncertainty with each additional  
534 constraint is expected to decrease as the total number of constraints increases. Finally,  
535 the impact of  $^{39}\text{Ar}$  data on the maximum entropy inversion will depend on the choice of  
536 prior. For example, if the prior already encodes the information contained in  $^{39}\text{Ar}$ , then  
537  $^{39}\text{Ar}$  would have no effect on the inversions. For the uniform and AD priors employed  
538 here,  $^{39}\text{Ar}$  provided additional constraints in about equal measure.

539 It is worth contrasting TTD estimates using the now popular parametric IG approach  
540 [e.g., *Waugh et al.*, 2003; *Huhn et al.*, 2008; *Tanhua et al.*, 2009; *DeVries and Primeau*,  
541 2010] to the ME approach employed here. The parametric approach assumes that the

542 TTD can be captured to a good approximation by an IG distribution that is completely  
543 specified by two parameters: its mean and variance, or equivalently,  $\Gamma$  and  $\Delta$ . With  
544 three transient tracer constraints, IG deconvolutions are thus formally overdetermined  
545 and the residual from a best fit could be used to estimate an uncertainty in the IG  
546 parameters. However, this apparent overdeterminedness is artificial for several reasons.  
547 First, the unimodal IG functional form cannot properly account for the mixing of different  
548 end-members, information that is encoded in tracers such as radiocarbon that have large  
549 spatial variations in their surface concentration. Indeed, the most probable shape of the  
550 TTDs as estimated by the ME deconvolutions is typically multimodal and not everywhere  
551 well-approximated by an IG. While a superposition of multiple IG functions could in prin-  
552 ciple take into account multiple end-members, the number of parameters that would need  
553 to be estimated from the data quickly exceeds the number of available tracer constraints.  
554 Second, the deconvolution is fundamentally highly underdetermined. Even if the tracer  
555 boundary conditions were spatially uniform, each radioactive tracer with decay constant  
556  $\lambda$  can be thought of as constraining only a single point of the Laplace transform of the  
557 TTD,  $\widehat{\mathcal{G}}(s) = \int_0^\infty \exp(-s\tau)\mathcal{G}(\tau)d\tau$ , at  $s = \lambda$ , underscoring the fact that the available  
558 tracer constraints leave the problem highly underdetermined. A key advantage of the ME  
559 deconvolutions is that it allowed us to estimate the uncertainty associated with this un-  
560 derdeterminedness. Legislating the TTD to be of IG form artificially suppresses the true  
561 uncertainty of the deconvolutions except for the case where there is certain prior knowl-  
562 edge that the TTD should closely follow the IG form. In this regard parametric inversions  
563 of tracer data for the TTD are analogous to the OMP method for determining water-mass  
564 fractions [e.g., *Tomczak*, 1981; *Tomczak and Large*, 1989] where the number of possible

565 end-members is fixed by hand, thereby artificially suppressing the underdetermined nature  
 566 of the data inversions [*Holzer et al.*, 2010].

## 7. Conclusions

567 The focus of this paper has been on the transit-time information provided by passive  
 568 oceanographic tracers when  $^{39}\text{Ar}$  measurements are used to bridge the gap between the  
 569 short-timescale CFCs and the long-timescale radiocarbon. To this end, we analyzed the  
 570 transient tracers CFC-11, CFC-12,  $^{39}\text{Ar}$ , and  $^{14}\text{C}$ , as well as the climatologically cyclo-  
 571 stationary scalars  $\theta$ ,  $S$ , and  $\text{PO}_4^*$ , which contain additional information on where a fluid  
 572 element was last in the mixed layer. The vastly underdetermined problem of deconvolving  
 573 the tracer concentrations at point  $\mathbf{r}$  for the mass fractions  $\mathcal{P}(s, \tau|\mathbf{r})$  that had a transit  
 574 time  $\tau$  from surface grid box  $s$  to  $\mathbf{r}$ , was regularized using a maximum-entropy method.  
 575 Because our focus is on the effect of  $^{39}\text{Ar}$ , which contains virtually no surface-origin infor-  
 576 mation, we limited analysis to the global integral of  $\mathcal{P}$  over surface origin, otherwise also  
 577 known as the TTD, its ideal mean age,  $\Gamma$ , and width,  $\Delta$ , and the mass fractions in spec-  
 578 ified transit-time bands. The uncertainties of these quantities were estimated from their  
 579 entropic probability distributions, neglecting uncertainties associated with the variability  
 580 of the tracer concentrations [*Holzer et al.*, 2010]. Our conclusions are as follows:

- 581 • Our ME deconvolutions revealed a spatial structure in the ideal mean age  $\Gamma$  and in  
 582 the water-mass fraction  $f_1$  with  $\tau \lesssim 105\text{a}$  that is consistent with the known distributions of  
 583 NADW, AAIW, and AABW in the Atlantic and with the simpler water-mass structure of  
 584 the Pacific. In addition to this qualitative consistency, our deconvolutions allowed us to  
 585 obtain quantitative estimates of  $\Gamma$ , the TTD width  $\Delta$ , and  $f_1$ , together with estimates of  
 586 their entropic uncertainties (Figures 6, 7, and 8). Inclusion of  $^{39}\text{Ar}$  led to reduced values

587 of  $f_1$  for the majority of the locations analyzed with mean ages that were correspondingly  
588 longer by about a century (Figures 13 and 14).

589 • For the Southern Ocean, a region of vigorous overturning where deep waters are both  
590 formed and upwelled, our ME deconvolutions produced TTDS with little depth dependence  
591 compared to other basins. At all depths, our inferred TTDS for the Southern Ocean had  
592 a mode at short transit times indicating the presence of newly ventilated waters and a  
593 long slowly decaying tail indicating the upwelling of old waters back to the surface.

594 • Having  $^{39}\text{Ar}$  available as an additional transient tracer tends to reduce the entropic  
595 uncertainty in our estimates of ideal mean age, TTD width, and water-mass fractions. For  
596 the water-mass fractions the reductions range on average from  $\sim 20\%$  to  $\sim 50\%$  depending  
597 on the transit-time band considered, and for ideal mean age the uncertainty is halved  
598 in the Southern Ocean with reductions of  $\sim 30\%$  elsewhere. With the uniform prior,  
599 including  $^{39}\text{Ar}$  either reduced or left unchanged the size of the entropic error bars at all  
600 locations. With the nonuniform AD prior, including  $^{39}\text{Ar}$  reduced the uncertainty for most  
601 locations, but for some bottles the uncertainty actually increased. Increases in uncertainty  
602 are typically accompanied by a substantial shift in the ME value of the diagnostic. Thus,  
603 while ME deconvolutions are guaranteed to uncover the true boundary propagator and its  
604 moments in the limit of an infinite number of tracer constraints, the reduction of entropic  
605 uncertainty in the approach to this limit can be non-monotonic with a nonuniform prior.

606 • The ME deconvolutions highlight the fact that TTDS generally do not have a simple  
607 unimodal IG form that is determined by only two parameters. Our ME deconvolutions  
608 do not fix the functional form of the TTD at the outset, which is reflected in substantial  
609 entropic uncertainties for mean age,  $\Gamma$ , and even greater uncertainties for the TTD width,

610  $\Delta$ . The ratio  $\Gamma/\Delta$  is also not as narrowly constrained as parametric inversions suggest  
611 [*Waugh et al.*, 2003; *Hall et al.*, 2004]. The implication is that IG-based estimates of  $\Gamma$   
612 and  $\Delta$  are insufficient to characterize transport from the surface because they ignore the  
613 large uncertainty associated with the underdetermined nature of the inversion.

614 • In the deep Pacific where CFCs have not yet penetrated, using both  $^{39}\text{Ar}$  and  $^{14}\text{C}$   
615 allows determination of a TTD with a realistic shape even when a uniform prior without  
616 any transit-time information is used. With only  $^{14}\text{C}$  and a uniform prior the ME solution  
617 would give a TTD with an unrealistic shape of a monotonically decreasing function with  
618 a non-zero value at  $\tau = 0$ .

619 • The additional transient tracer  $^{39}\text{Ar}$  gives the maximum-entropy solution for the  
620 boundary propagator additional freedom. In the case of the uniform prior, having only  
621 CFCs and radiocarbon unrealistically constrains the mode of the propagator to lie within  
622 the CFC period ( $\sim 70\text{a}$ ) regardless of the tracer concentrations. Including  $^{39}\text{Ar}$  relaxes  
623 this constraint so that even with a uniform prior the deconvolved TTD is free to place its  
624 mode at any transit time.

625 • The Pacific profiles come closest to approximating the behavior of simple 1d  
626 advection-diffusion, particularly below the thermocline where the TTDs become unimodal  
627 with a shape that is at least roughly approximated by an IG functional form. In the case  
628 of the ME inversions with the uniform prior for the Pacific data, the effect of including  
629  $^{39}\text{Ar}$  on the estimated water-mass fractions in a given transit-time interval is similar to  
630 the effect seen for a simple 1d model with synthetic data generated by an IG TTD.

631 • Remarkably,  $^{39}\text{Ar}$  in combination with the other six tracers already provides a suffi-  
632 cient number of constraints to make the inversions relatively insensitive to the choice of

633 prior. Deconvolutions using either the uniform or AD prior give similar results both in  
634 the case of the mass-fraction of water with transit times less than  $\sim 100$ a and in the case  
635 of ideal mean age.

636 Using  $^{39}\text{Ar}$  as an additional transient tracer led to substantial changes in our ME esti-  
637 mates of ideal mean age, TTD width, and water-mass fractions, while at the same time  
638 reducing their entropic uncertainties. There is no question that an effort to produce a  
639 globally gridded  $^{39}\text{Ar}$  data set would greatly help reduce the uncertainty in our knowl-  
640 edge of oceanic transport and ventilation, which in turn would greatly benefit rigorous  
641 estimates of the ocean's ability to take up and sequester anthropogenic carbon.

642 **Acknowledgments.** This work was supported by NSF grants OCE-0727229  
643 (Columbia) and OCE-0726871 (UC Irvine). We thank Bill Smethie for discussions and  
644 for making the thesis of *Rodriguez* [1993] available to us.

## Appendix A: Numerical details

645 For the inversions with the oceanographic data (as opposed to the 1d model), transit  
 646 time was resolved as follows:  $\tau \in [0, 3, 6, \dots, 75, 80, 90, 120, 160, 200, 250, 300, 400, \dots,$   
 647  $1000, 1200, 1500, 2000, \dots, 4000, 5000, 7000, 9000, 11000, 15000, 20000]$ a. Integrations  
 648 over transit-time bands were performed by zeroing  $\tau \in [120, 20000]$ a for band one,  $\tau \in$   
 649  $[0, 90] \cup [600, 20000]$ a for band two, and  $\tau \in [600, 20000]$ a for band three, followed by  
 650 trapezoidal integration over all transit times. Thus, for example, the edge of the youngest  
 651 transit-time band has a linear taper from 90 to 120a. The approximate boundaries between  
 652 the transit-time bands therefore lie at 105 and 550a.

## Appendix B: Uncertainty propagation

653 While entropic uncertainties in moments of the TTD's can straightforwardly be com-  
 654 puted, uncertainties in nonlinear functions of these moments are more difficult to com-  
 655 pute. Here we approximate the error in the TTD width  $\Delta \equiv \sqrt{(m_2 - \Gamma^2)/2}$  by making  
 656 the ansatz that the uncertainties in the mean age (first moment) and in the second mo-  
 657 ment  $m_2 \equiv \int_0^\infty \tau^2 \mathcal{G}(\tau) d\tau$  can be treated as statistically independent for the purpose of  
 658 estimating the error in  $\Delta$ . Given uncertainties  $\delta\Gamma$  and  $\delta m_2$ , we therefore approximate the  
 659 error in  $\Delta$  as  $\delta\Delta = \sqrt{(\partial\Delta/\partial\Gamma)^2(\delta\Gamma)^2 + (\partial\Delta/\partial m_2)^2(\delta m_2)^2}$ . Asymmetric error bounds for  
 660  $\Delta$  were calculated by separately using the right and left entropic error bars calculated for  
 661  $\Gamma$  and  $m_2$ .

662 The uncertainty bounds on the ratio  $\Gamma/\Delta$  was estimated roughly as  $[\Gamma_{min}/\Delta_{max}, \Gamma_{max}/\Delta_{min}]$ ,  
 663 where  $[\Gamma_{min}, \Gamma_{max}]$  are the probability bounds on the entropic uncertainty of the mean age  
 664 (the left and right limits of our entropic error bars), and  $[\Delta_{min}, \Delta_{max}]$  are the uncertainty  
 665 bounds calculated as described in the previous paragraph.

## References

- 666 Antonov, J. I., R. A. Locarnini, T. P. Boyer, A. V. Mishonov, and H. E. Garcia, World  
667 Ocean Atlas 2005, Volume 2: Salinity. S. Levitus, Ed., *NOAA Atlas NESDIS 62, U.S.*  
668 *Government Printing Office, Washington, D.C.*, p. 182pp, 2006.
- 669 Broecker, W., and T.-H. Peng, Comparison of  $^{39}\text{Ar}$  and  $^{14}\text{C}$  ages for waters in the deep  
670 ocean, *Nuclear Instruments and Methods in Physics Research B*, *172*, 473–478, 2000.
- 671 Broecker, W. S., et al., How much deep water is formed in the Southern Ocean?, *J.*  
672 *Geophys. Res.*, *103*, 15,833–25,843, 1998.
- 673 DeVries, T., and F. Primeau, An improved method for estimating water-mass ventilation  
674 age from radiocarbon measurements, *Earth and Planetary Science Letters*, *in press.*  
675 <http://www.ess.uci.edu/~fprimeau/publications.html>, 2010.
- 676 Foster, T. D., and E. C. Carmack, Frontal zone mixing and Antarctic Bottom Water  
677 formation in the southern Weddell Sea, *Deep-Sea Research*, *23*, 301–317, 1976.
- 678 Gaelens, M., M. Loiselet, G. Ryckewaert, R. C. Pardo, R. H. Scott, R. Vondrasek, P. Col-  
679 lon, and W. Kutchera, Oceans circulation and electron cyclotron resonance sources:  
680 Measurement of the ar-39 isotopic ratio in seawater, *Rev. Sci. Instrum.*, *75*, 1916, 2005.
- 681 Garcia, H. E., R. A. Locarnini, T. P. Boyer, and J. I. Antonov, World ocean atlas 2005,  
682 Volume 3: Dissolved oxygen, apparent oxygen utilization, and oxygen saturation. S.  
683 Levitus Ed., *NOAA Atlas NESDIS 63, U.S. Government Printing Office, Washington,*  
684 *D.C.*, p. 342pp, 2006a.
- 685 Garcia, H. E., R. A. Locarnini, T. P. Boyer, and J. I. Antonov, World ocean atlas 2005,  
686 Volume 4: Nutrients (phosphate, nitrate, silicate). S. Levitus Ed., *NOAA Atlas NESDIS*  
687 *64, U.S. Government Printing Office, Washington, D.C.*, p. 396pp, 2006b.

- 688 Gehrie, E., D. Archer, S. Emerson, C. Stump, and C. Henning, Subsurface ocean argon  
689 disequilibrium reveals the equatorial Pacific shadow zone, *J. Geophys. Res.*, *33*, 2006.
- 690 Gull, S. F., and G. J. Daniell, Image reconstruction from incomplete and noisy data,  
691 *Nature*, *272*, 686–690, 1978.
- 692 Hall, M. M., T. M. Joyce, R. S. Pickart, W. M. Smethie, and D. J. Torres, Zonal circulation  
693 across 52°w in the north atlantic, *J. Geophys. Res.*, *109*, 2004.
- 694 Hall, T. M., and R. A. Plumb, Age as a diagnostic of stratospheric transport, *J. Geophys.*  
695 *Res.*, *99*, 1259–1070, 1994.
- 696 Holzer, M., and T. M. Hall, Transit-time and tracer-age distributions in geophysical flows,  
697 *J. Atmos. Sci.*, *57*, 3539–3558, 2000.
- 698 Holzer, M., F. W. Primeau, W. M. Smethie, and S. Khatiwala, Where and how long  
699 ago was water in the western North Atlantic ventilated? Maximum-entropy inver-  
700 sions of bottle data from WOCE line A20, *Journal of Geophysical Research*, *in press*  
701 <http://web.maths.unsw.edu.au/~markholzer>, 2010.
- 702 Huhn, O., W. Roether, and R. Steinfeldt, Age spectra in North Atlantic Deep Water  
703 along the South American continental slope, 10°N 30°S, based on tracer observations,  
704 *Deep-Sea Research I*, *55*, 1252–1276, 2008.
- 705 Jaynes, E. T., Information Theory and Statistical Mechanics, *Physical Review*, *106*, 620–  
706 630, 1957.
- 707 Key, R. M., et al., A global ocean carbon climatology: Results from GLODAP, *GBC*, *18*,  
708 2004.
- 709 Locarnini, R. A., A. V. Mishonov, J. I. Antonov, T. P. Boyer, and H. E. Garcia, World  
710 Ocean Atlas 2005, Volume 1: Temperature. S. Levitus, Ed., *NOAA Atlas NESDIS 61*,

- 711 *U.S. Government Printing Office, Washington, D.C.*, p. 182pp, 2006.
- 712 Loosli, H. H., A dating method with  $^{39}\text{Ar}$ , *Earth Planet. Sci. Lett.*, *63*, 51–62, 1983.
- 713 Loosli, H. H.,  $^{39}\text{Ar}$ : A tool to investigate ocean water circulation and mixing, in *Hand-*  
714 *book of Environmental Isotope Chemistry, Vol. 3, The Marine Environment*, edited by  
715 P. Fritz and C. Fontes, pp. 385–392., Elsevier, New York, 1989.
- 716 Luyten, J. R., J. Pedlosky, and H. Stommel, The Ventilated Thermocline, *J. Phys.*  
717 *Oceanog.*, *13*, 292–309, 1983.
- 718 Maier-Reimer, E., Geochemical cycles in an ocean general circulation model. Preindustrial  
719 tracer distributions, *Global Biogeochem. Cycles*, *7*, 645–677, 1993.
- 720 Orsi, A. H., G. C. Johnson, and J. L. Bullister, Circulation, mixing, and production of  
721 Antarctic Bottom Water, *Progress In Oceanography*, *43*, 55–109, 1999.
- 722 Press, W., S. Teukolsky, W. Vetterling, and B. Flannery, *The Art of Scientific Computing*,  
723 3rd ed., Cambridge University Press, 2007.
- 724 Rodriguez, J., Beitrage zur Verteilung von  $^{39}\text{Ar}$  im Atlantik, Ph.D. Thesis: Inauguraldis-  
725 sertation der Philosophisch-naturwissenschaftlichen Fakultät der Universität Bern zur  
726 Erlangung der Doktorwurde, Universität Bern, Switzerland, 1993.
- 727 Sabine, C. L., R. M. Key, A. Kozyr, R. A. Feely, R. Wanninkhof, F. J. Millero, T.-  
728 H. Peng, J. L. Bullister, and K. Lee, Global Ocean Data Analysis Project: Results  
729 and data. ORNL/CDIAC-145, ndp-083, *Carbon Dioxide Information Analysis Center*,  
730 *Oak Ridge National Laboratory, U.S. Department of Energy, Oak Ridge, Tennessee*, p.  
731 110pp, 2005.
- 732 Schlitzer, R., W. Roether, U. Weidmann, P. Kalt, and H. H. Loosli, A Meridional  $^{14}\text{C}$   
733 and  $^{39}\text{Ar}$  Section in Northeast Atlantic Deep Water, *J. Geophys. Res.*, *90*, 6945–6952,

- 1985.
- Shannon, C. E., Prediction and entropy of printed English, *The Bell System Technical Journal*, *30*, 50–64, 1951.
- Skilling, J., and S. F. Gull, Bayesian maximum entropy image reconstruction, in *Spatial statistics and imaging: Papers from the Research Conference on Image Analysis and Spatial Statistics held at Bowdoin College, Brunswick, Maine, Summer 1988*, edited by A. Possolo, pp. 341–367, Institute of Mathematical Statistics, Hayward, CA, 1991.
- Tanhua, T., E. P. Jones, E. Jeansson, S. Jutterström, W. M. S. Jr., D. W. R. Wallace, and L. G. Anderson, Ventilation of the Arctic Ocean: Mean ages and inventories of anthropogenic CO<sub>2</sub> and CFC-11, *J. Geophys. Res.*, *114*, 2009.
- Tomczak, M., A multiparameter extension of temperature/salinity diagram techniques for the analysis of non-isopycnal mixing, *Prog. Oceanogr.*, *10*, 147–171, 1981.
- Tomczak, M., and D. G. Large, Optimum multiparameter analysis of mixing in the thermocline of the eastern indian ocean, *J. Geophys. Res.*, *94*, 16,141–16,149, 1989.
- Walker, S. J., R. F. Weiss, and P. K. Salameh, Reconstructed histories of the annual mean atmospheric mole fractions for the halocarbons CFC-11, CFC-12, CFC-113 and carbon tetrachloride, *J. Geophys. Res.*, *105*, 14,285–14,296, 2000.
- Waugh, D. W., T. M. Hall, and T. W. N. Haine, Relationships among tracer ages, *J. Geophys. Res.*, *108*, 3138, 2003.
- Waugh, D. W., T. W. N. Haine, and T. M. Hall, Transport times and anthropogenic carbon in the subpolar North Atlantic ocean, *Deep Sea Res. I*, *51*, 1475–1491, 2004.
- Waugh, D. W., T. M. Hall, B. I. . McNeil, R. Key, and R. J. . Matear, Anthropogenic CO<sub>2</sub> in the oceans estimated using transit time distributions, *Tellus*, *58B*, 376–389, 2006.

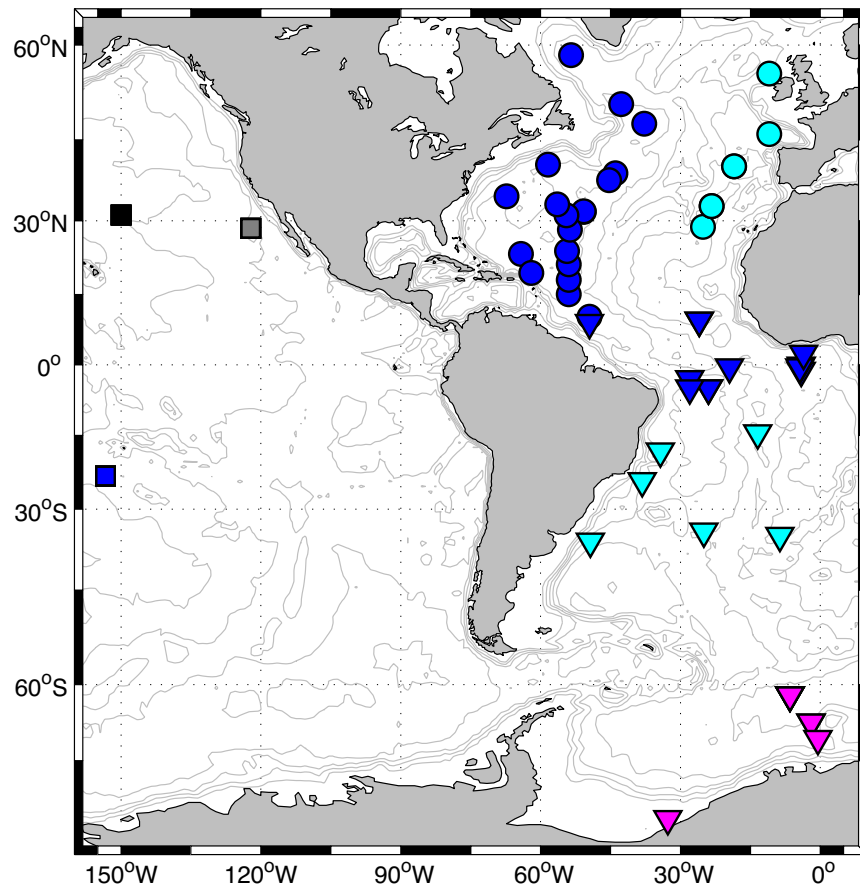


**Figure 1.** The locations of the  $^{39}\text{Ar}$  measurements used in this study. Symbol shapes and colors are introduced to label different regions. Bathymetry is indicated in 1000-m intervals.

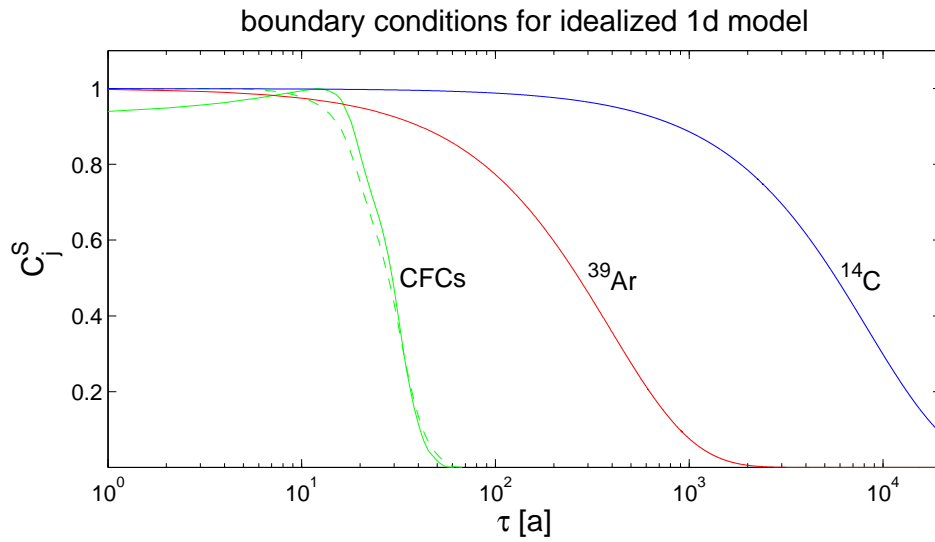


**Figure 2.** The effective surface boundary conditions for the idealized 1d model as a function of time since last surface contact,  $\tau$ , for the four transient tracers considered: CFC-11 (green, solid), CFC-12 (green, dashed),  $^{39}\text{Ar}$  (red),  $^{14}\text{C}$  (blue). The logarithmic time axis emphasizes that the  $^{39}\text{Ar}$  timescale is roughly the geometric mean of the CFC and  $^{14}\text{C}$  timescales.

## maximum-entropy TTDS for idealized 1d model

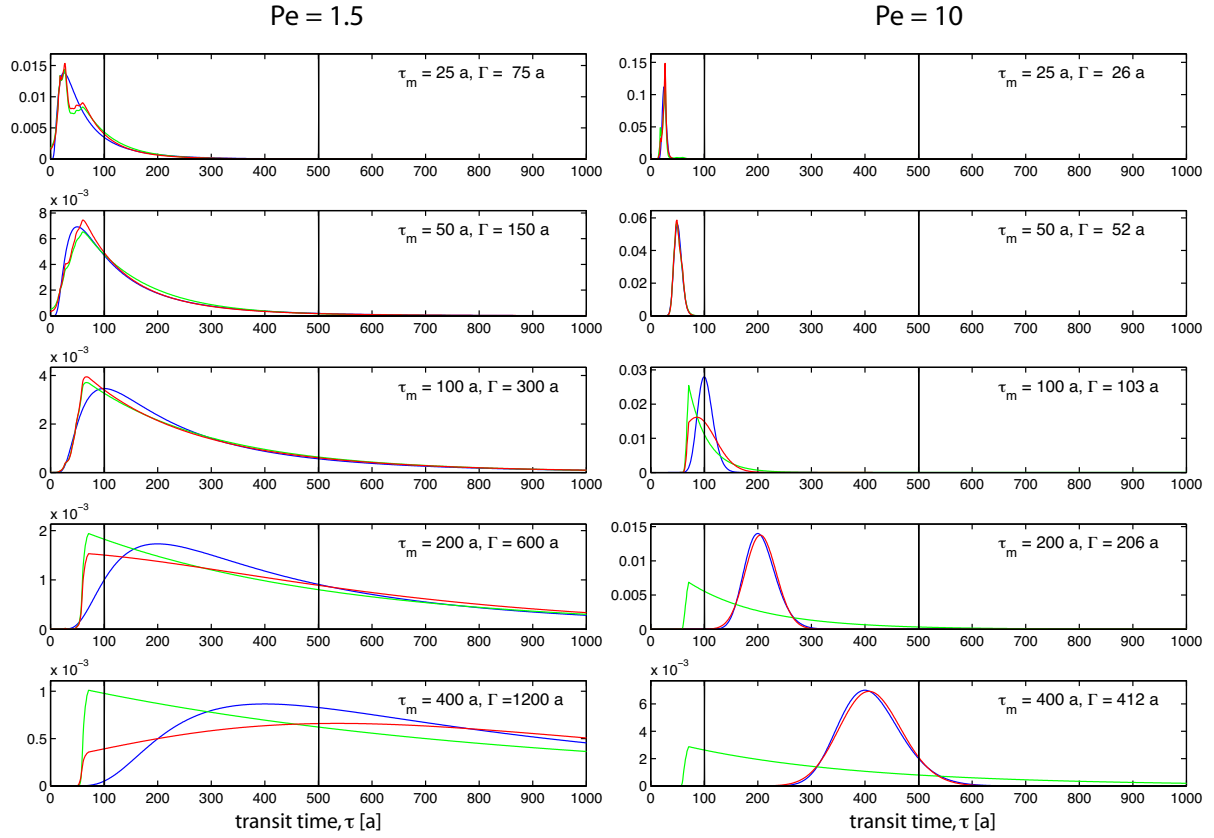


**Figure 3.** The ME TTD solutions for the idealized 1d model. The ME TTDs are plotted in green (no  $^{39}\text{Ar}$ ) and red (with  $^{39}\text{Ar}$ ), while the underlying exact TTDs are plotted in blue. The exact TTDs were convolved with the idealized boundary conditions of Figure 2 to generate the synthetic tracer data used by the ME inversions. The exact TTDs on the left are characterized by  $Pe = 1.5$ , while those on the right are more advective with  $Pe = 10$ . For each  $Pe$ , five exact TTDs with different mean ages  $\Gamma$  (and hence different modes,  $\tau_m$ ) were used as indicated. The vertical black lines are the boundaries of the three transit-time bands considered to define  $\tau$ -integrated water-mass fractions.

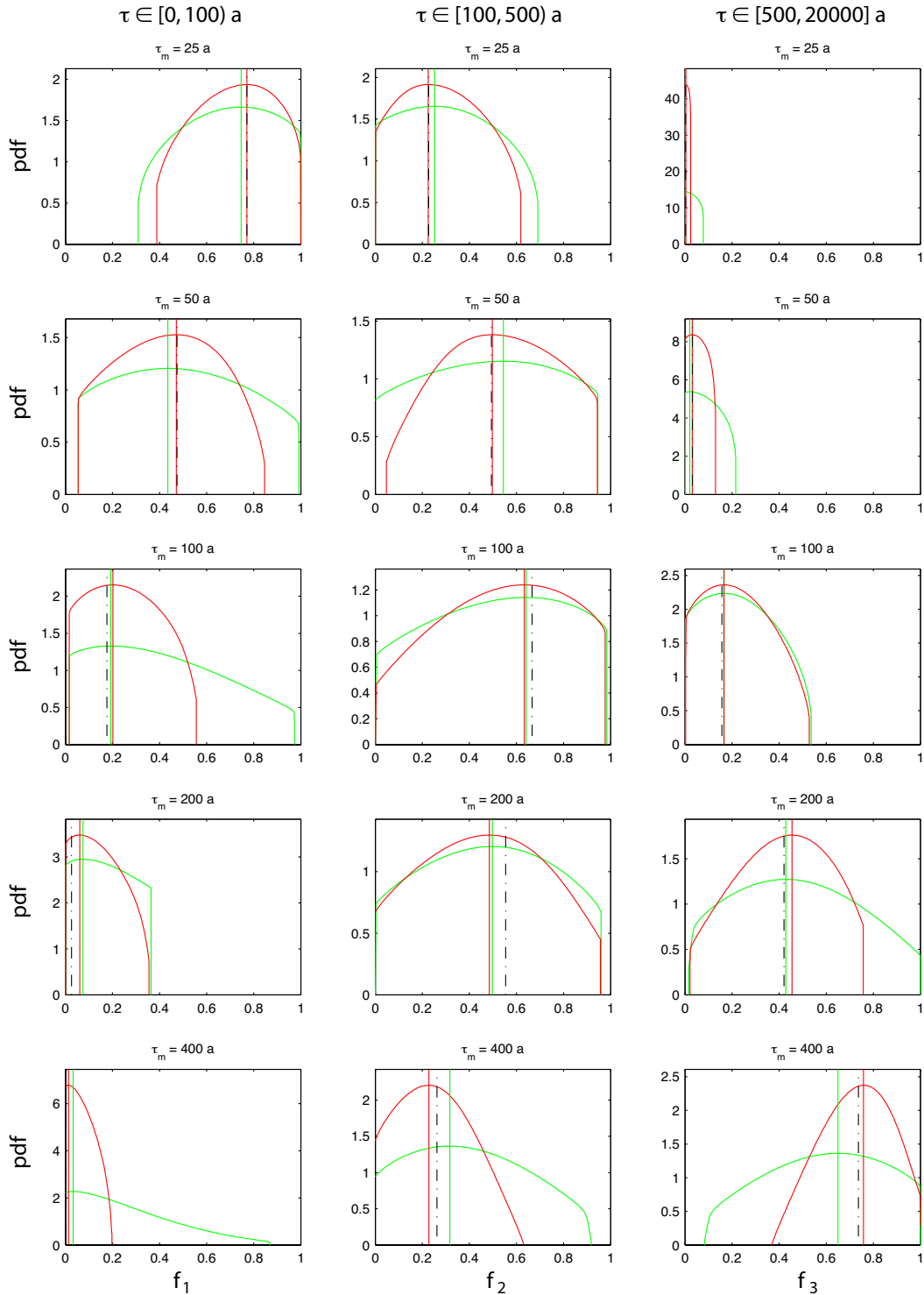


**Figure 4.** The entropic pdfs of the water-mass fractions in the three transit-time bands  $\tau \in [0, 100]a$ ,

$\tau \in [100, 500]a$ , and  $\tau \in [500, 20000]a$  for the idealized 1d model with  $Pe = 1.5$  (green for the case without  $^{39}\text{Ar}$ ,

red for the case with  $^{39}\text{Ar}$ ). Each row of plots is for a different underlying assumed IG boundary propagator

characterized by the modes  $\tau_m$  indicated (for  $Pe = 1.5$  one has  $\Gamma = 3\tau_m$ ). The black dot-dashed vertical lines

indicate the exact water-mass fractions of the IG propagators, and the green and red vertical lines indicate the

maximum-entropy values at the maxima of the corresponding pdfs.

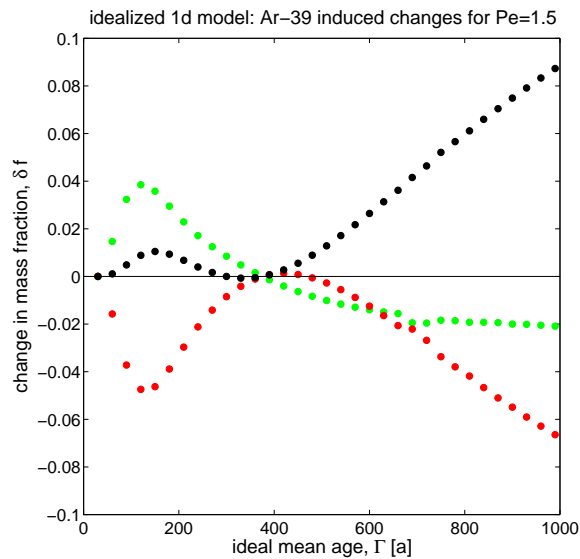


**Figure 5.** The change,  $\delta f$ , of the water-mass fractions (with  $^{39}\text{Ar}$  minus without  $^{39}\text{Ar}$ ) in each transit-time band for the idealized 1d model with  $Pe = 1.5$  as a function of the true mean age,  $\Gamma$ , of the underlying TTD. The change in the water-mass fraction with  $\tau \in [0, 100)\text{a}$  is plotted in green, with  $\tau \in [100, 500)\text{a}$  in red, and with  $\tau \in [500, 20000]\text{a}$  in black.

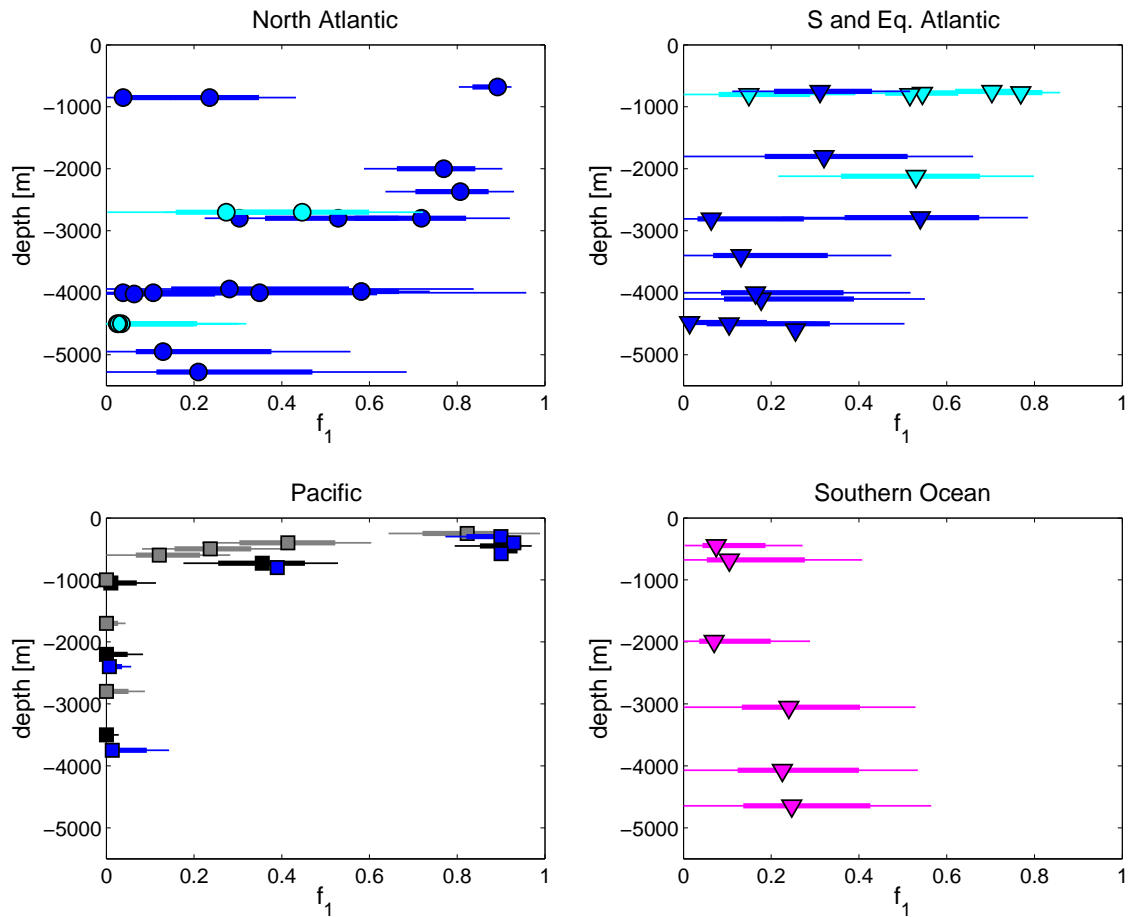


**Figure 6.** The mass fraction  $f_1$  of water with transit time  $\tau \in [0, 105)$  a as determined using  $^{39}\text{Ar}$  and the AD prior. Thick error bars cover half the probability of the associated entropic distribution, and thin error bars are associated with the width at half maximum of these distributions. Symbol shapes and colors identify the location of the  $^{39}\text{Ar}$  measurements as in Figure 1.

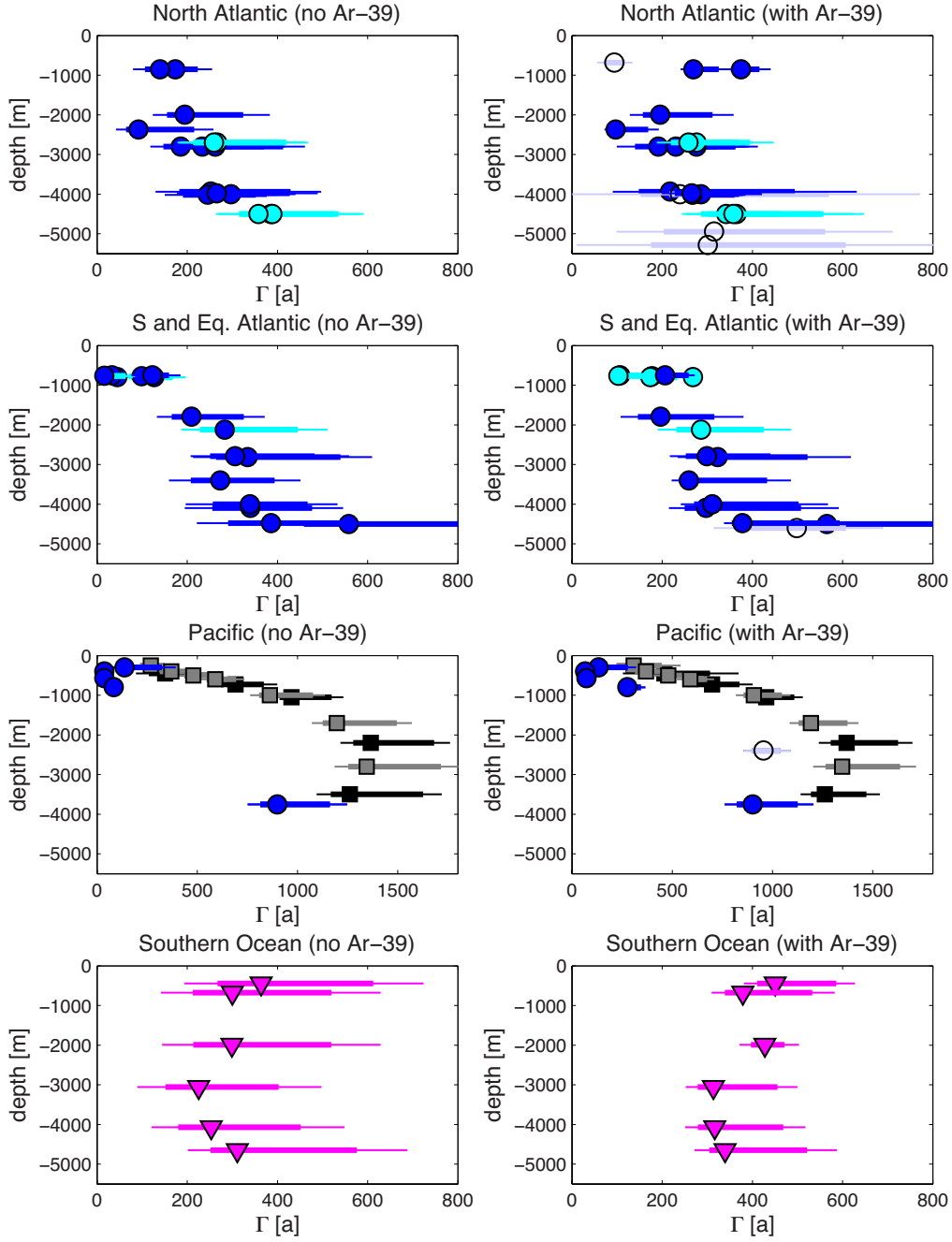


**Figure 7.** The ideal mean age,  $\Gamma$ , with (right panels) and without (left panels)  $^{39}\text{Ar}$  and the AD prior. Thick error bars cover half the probability of the associated entropic distribution, and thin error bars are associated with the width at half maximum of these distributions. Symbol shapes and colors identify the location of the  $^{39}\text{Ar}$  measurements as in Figure 1. Note that the Pacific has a different age scale. For  $\Gamma$  obtained with  $^{39}\text{Ar}$ , open symbols with error bars in lighter color (four Atlantic and one Pacific location) indicate that the corresponding estimate without  $^{39}\text{Ar}$  was not available due to numerical problems.

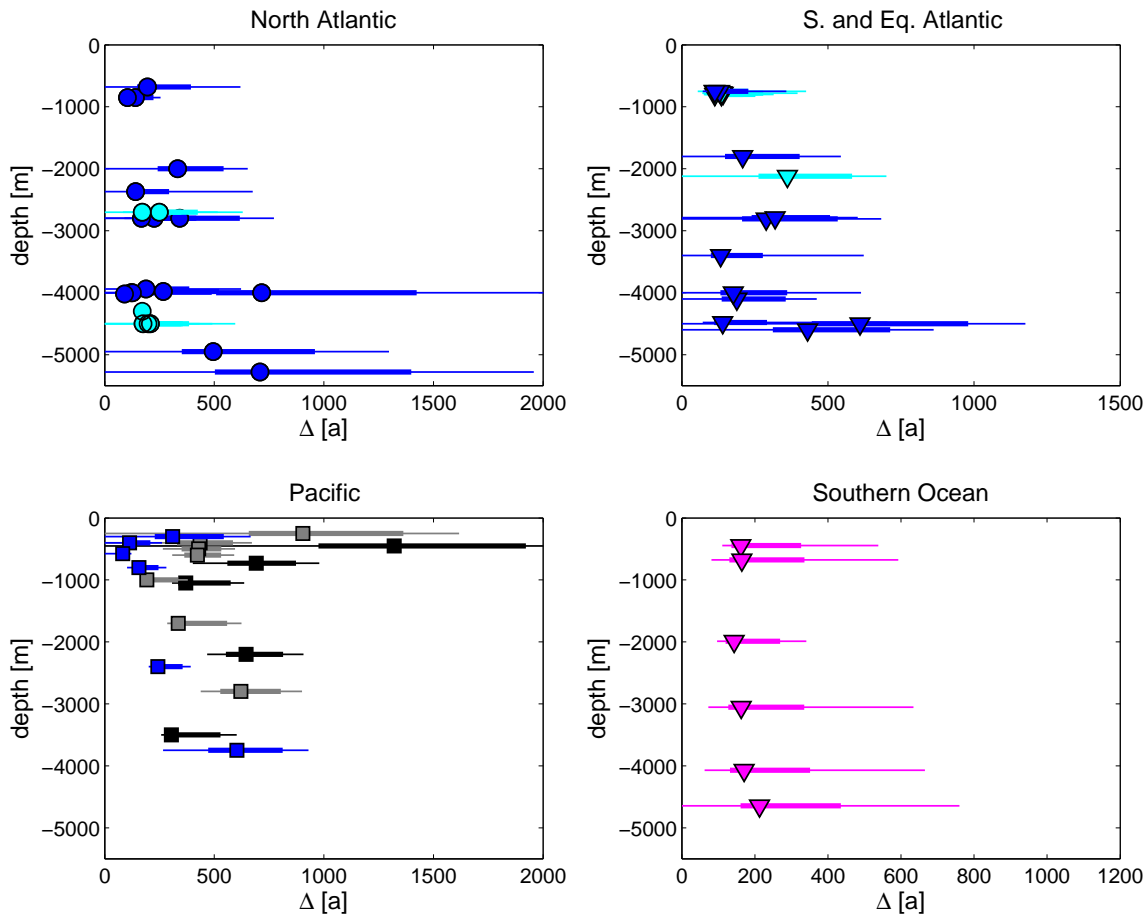


**Figure 8.** The TTD width,  $\Delta$ , using  $^{39}\text{Ar}$  and the model prior. Error bars were estimated as discussed in Appendix B. Symbol shapes and colors identify the location of the  $^{39}\text{Ar}$  measurements as in Figure 1. Note that different basins have different scales for  $\Delta$ .

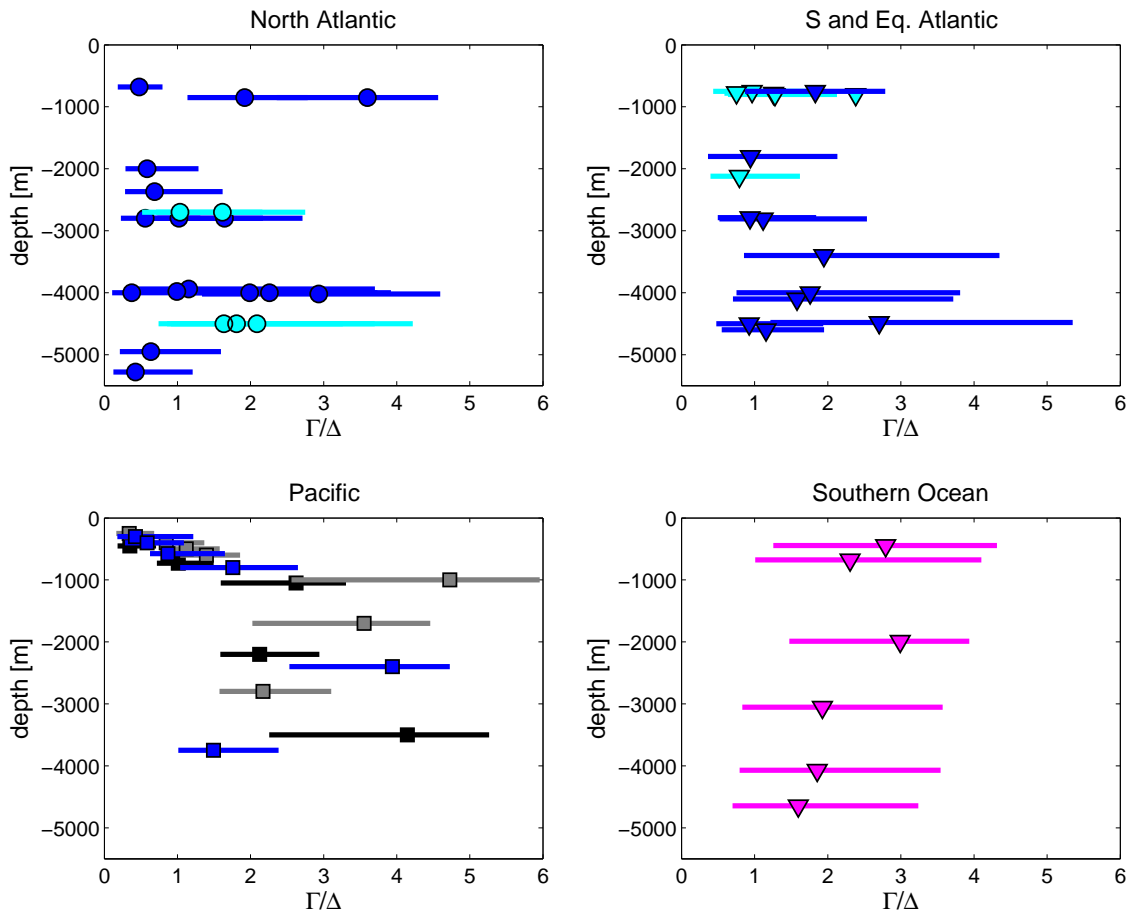


**Figure 9.** The fraction  $\Gamma/\Delta$  for the inversions with the AD prior and  $^{39}\text{Ar}$ . Error bars were estimated as discussed in Appendix B. Symbol shapes and colors identify the location of the  $^{39}\text{Ar}$  measurements as in Fig. 1.

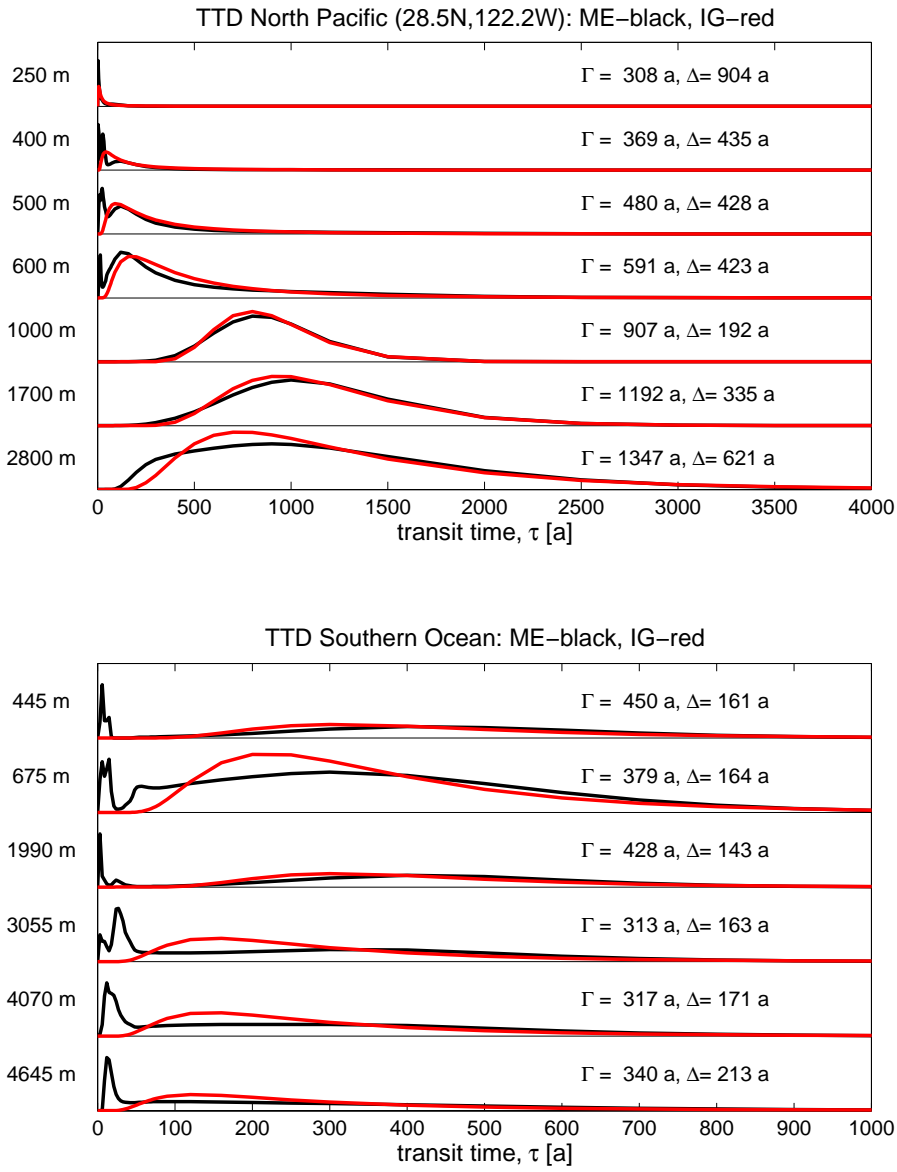


**Figure 10.** The global TTDs for the Pacific profile at 28.5°N, 122.2°W (upper plot), and for the Southern Ocean data (lower plot). The black curves correspond to the ME solutions, while the red curves are inverse Gaussians of the same ideal mean age,  $\Gamma$ , and width,  $\Delta$ , as indicated next to the curves. Every pair of ME TTD and corresponding inverse Gaussian has been normalized by the peak value of the ME TTD.

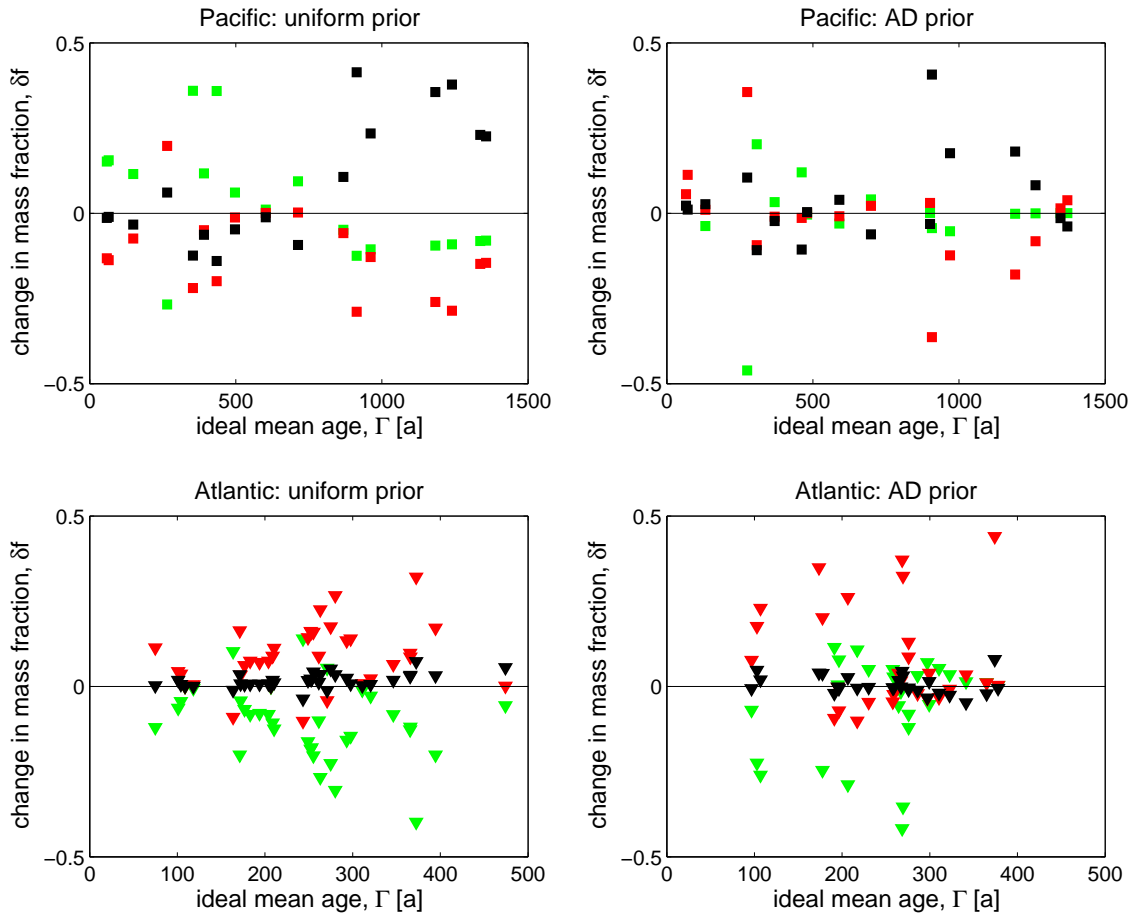


**Figure 11.** The change of the mass fraction,  $\delta f$ , (with  $^{39}\text{Ar}$  minus no  $^{39}\text{Ar}$ ) in each of the three transit-time bands considered (short- $\tau$  in green, mid- $\tau$  in red, long- $\tau$  in black) versus ideal mean age (determined with  $^{39}\text{Ar}$ ) for the Pacific and Atlantic bottles. The uniform prior case is shown on the left and AD prior case on the right.

Note the different age scales for the Pacific and Atlantic.

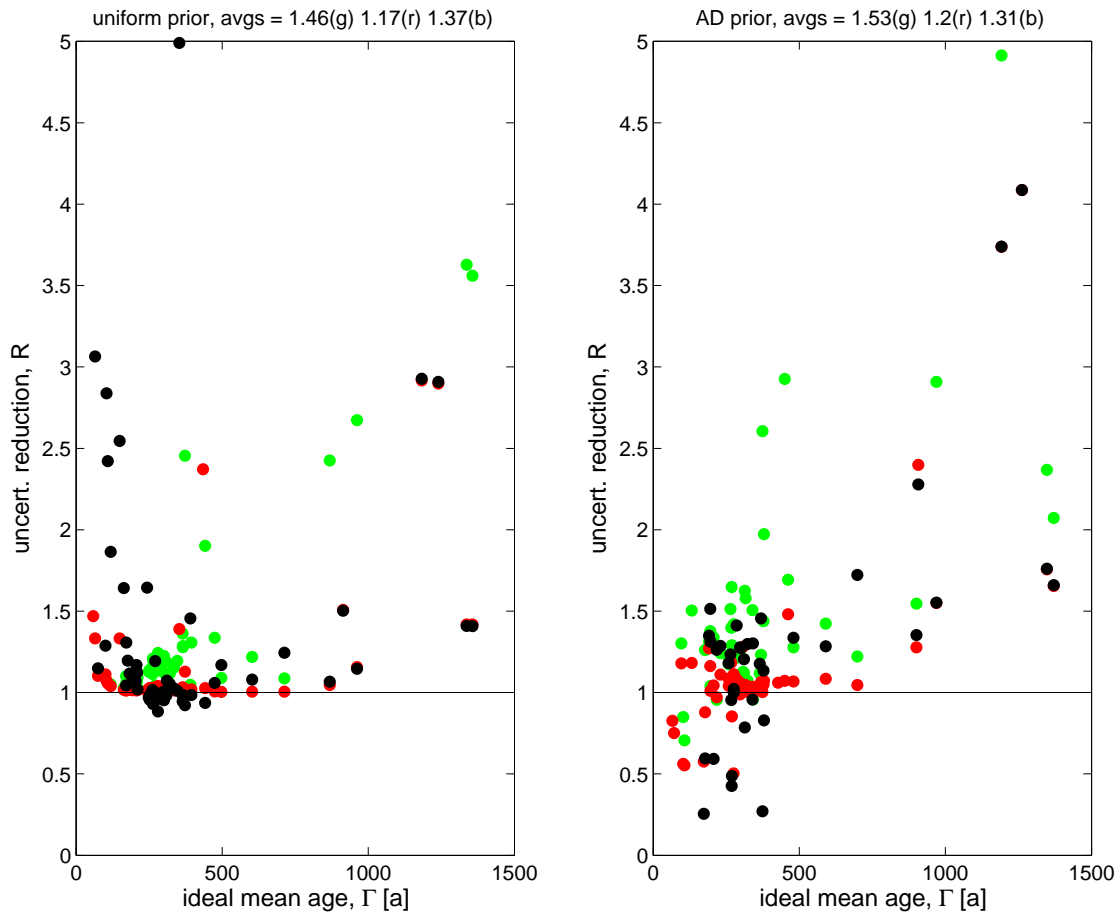


**Figure 12.** The reduction of the entropic uncertainty in the mass fraction in each transit-time band (short- $\tau$  in green, mid- $\tau$  in red, long- $\tau$  in black) as a function of ideal mean age,  $\Gamma$ . The uncertainty reduction is defined as the ratio,  $R$ , of the size of the entropic quartile error bar without  $^{39}\text{Ar}$  to the size of the quartile error bar when  $^{39}\text{Ar}$  is included. The reduction  $R$  is plotted as function of the mean age of the bottle (determined with  $^{39}\text{Ar}$  included) for the case of the uniform prior (left) and AD prior (right), and the mean value of  $R$  for the bottles for which  $R \geq 1$  is indicated in the title for each transit-time band (g: short- $\tau$ , r: mid- $\tau$ , b: long- $\tau$ ).

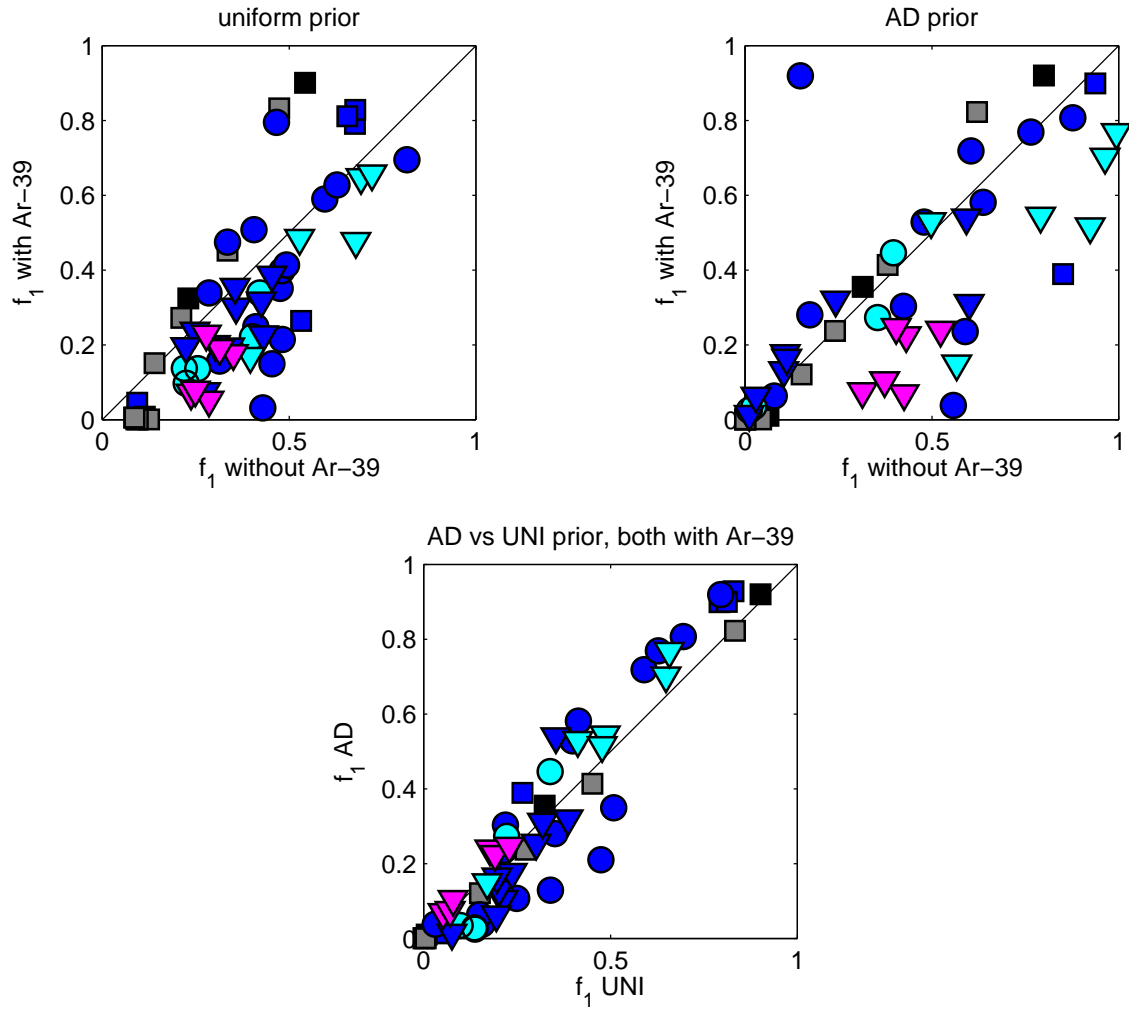


**Figure 13.** The top two plots show the mass fraction  $f_1$  of water with transit time  $\tau \in [0, 105)a$ , as computed with  $^{39}\text{Ar}$  versus the same quantity computed without  $^{39}\text{Ar}$  for the cases of uniform and AD prior, as indicated. The bottom plot shows  $f_1$  computed with the AD prior versus  $f_1$  computed with the uniform prior, both with  $^{39}\text{Ar}$ . Symbol shapes and colors identify the location of the  $^{39}\text{Ar}$  measurements as in Figure 1.

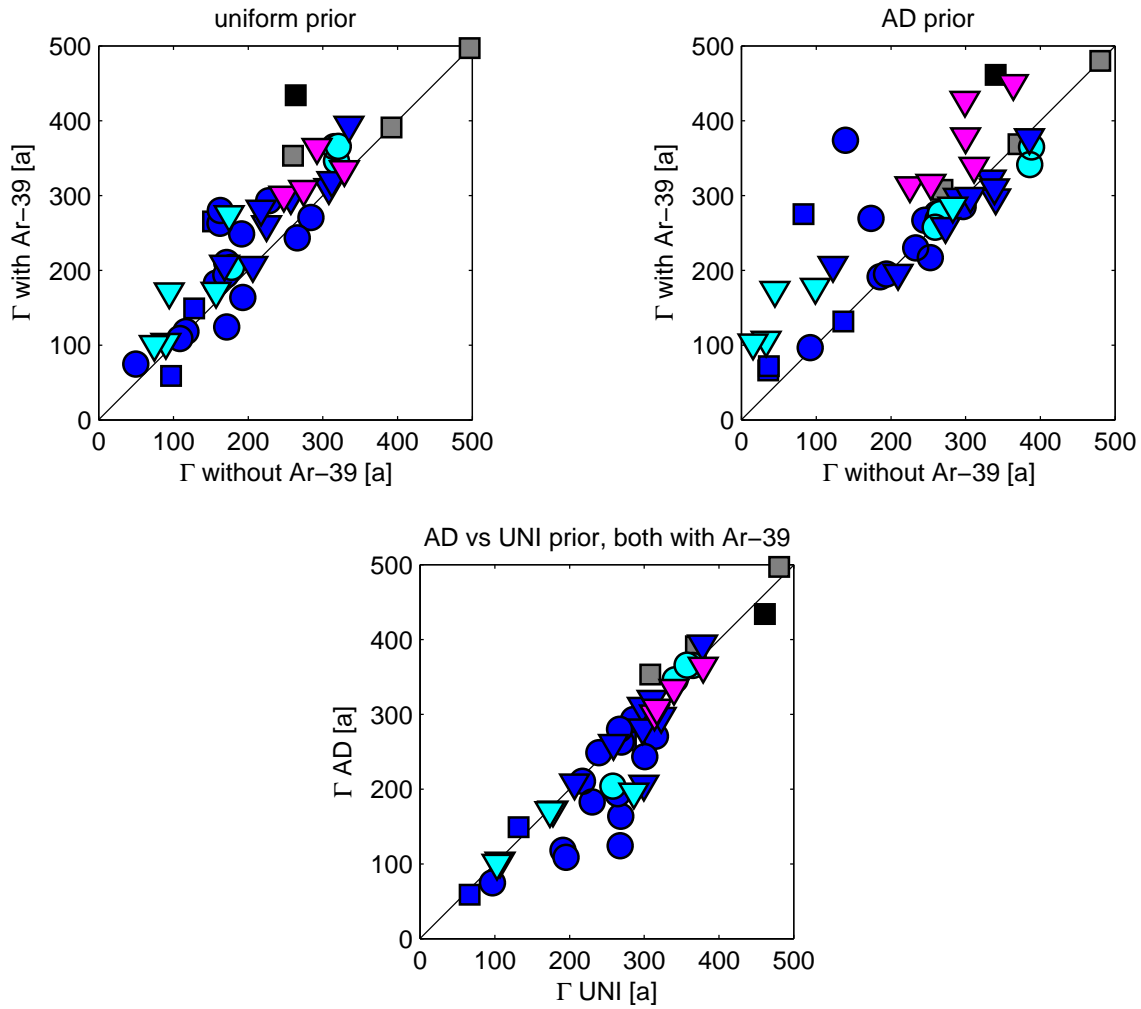


**Figure 14.** Ideal mean age,  $\Gamma$ , with  $^{39}\text{Ar}$  versus  $\Gamma$  without  $^{39}\text{Ar}$  as determined by the ME deconvolutions.

The bottom plot shows  $\Gamma$  computed with the AD prior versus  $\Gamma$  computed with the uniform prior, both with  $^{39}\text{Ar}$ .

Symbol shapes and colors identify the location of the  $^{39}\text{Ar}$  measurements as in Figure 1.